https://doi.org/10.5194/egusphere-2025-3404
Preprint. Discussion started: 29 July 2025

Volume-to-extinction ratio: An important property of dust

Alkistis Papetta[1], Maria Kezoudi[1], Holger Baars[2], Athina Floutsi[2], Eleni Drakaki[3], Konrad Kandler[4], Elena Louca[1], Theodoros Christoudias[1], Eleni Marinou[3], Chris Stopford[5], Troy Thornberry [6], Vassilis Amiridis[3], Jean Sciare[1], and Franco Marenco[1]

[1] Climate and Atmosphere Research Centre (CARE-C), The Cyprus Institute, Nicosia 2121, Cyprus
[3]Institute for Astronomy, Astrophysics, Space Applications and Remote Sensing, National Observatory of Athens, Athens, 15236, Greece
[2]Leibniz Institute for Tropospheric Research (TROPOS), 04318 Leipzig, Germany
[4]Institute of Applied Geosciences, Technical University of Darmstadt, Darmstadt 64287, Germany
[5]University of Hertfordshire, Hatfield, United Kingdom
[6]National Oceanic Atmospheric Administration (NOAA), Boulder, CO 80305, USA

Correspondence: Alkistis Papetta (a.papetta@cyi.ac.cy)

Abstract. The volume-to-extinction ratio (ζ) is an important aerosol property, allowing to relay gravimetric and optical quantifications, widely used in remote sensing and in climate models. The ζ parameter is affected by the microphysical properties of aerosol particles, including their size, shape and composition . This study presents a novel, synergistic approach combining airborne in-situ observations and ground-based remote sensing to study this parameter during dust events originating in the Middle East and Saharan regions, and examine its variability and general estimation uncertainty. The data were collected during the 2021 Cyprus Fall Campaign and the 2022 ASKOS campaign in Cabo Verde. The combination of observations offered vertically-resolved observations of the particle size-distribution and volume-to-extinction ratio. The findings of this study reveal significant variability in the ζ parameter and the effective radius across different events and regions. During Middle East dust events in Cyprus the observed average ζ was the lowest with $\zeta = 0.53 \pm 0.24\,\mu m$, whilst for a Saharan dust case in Cabo Verde observations showed the highest values with $\zeta = 1.14 \pm 1.01\,\mu m$, both at the dust layer altitude. The analysis highlights large discrepancies compared to AERONET-derived values and previous literature, especially in the presence of coarse and giant particles. Scattering computations allowed to evaluate the experimental results and provide insights into the role of particle asphericity. Atmospheric model simulations also showed discrepancies, mainly due to assumptions that neglect larger particles. These findings suggest that improve dust representation in models is essential for accurate climate assessment.

1 Introduction

Understanding whether aerosols warm or cool the planet is key to explaining, mitigating, and predicting climate change (IPCC, 2021). Many studies over the past decades have explored this question, which is challenging due to the various ways aerosols interact with radiative forcing. Firstly, aerosols can interact (directly) with solar and terrestrial radiation, either scattering light to produce a cooling effect or absorbing it to contribute to warming. Beyond their direct effect on radiation, aerosols also have an indirect impact by influencing cloud formation by acting as cloud condensation nuclei (CCN) and ice-nucleating particles

(INP), altering cloud properties and precipitation patterns (Albrecht, 1989; Karydis et al., 2017). Adding to the complexity, natural aerosol emissions, such as dust, are not fixed; they respond dynamically to climate changes, amplifying or dampening atmospheric feedbacks (Carslaw et al., 2010).

The interaction of aerosols with radiation is dependent on their optical and microphysical properties (e.g. particle size, refractive index), which vary based on composition, source, and atmospheric processing. For example, sulfate and nitrate aerosols, typically smaller than 1 μm, primarily scatter radiation due to the low imaginary part of their refractive index, leading to cooling effects (Robock, 2000; Zaehle et al., 2011). In contrast, black carbon (BC), with particle sizes of 0.1–0.25 μm, are good absorbers of shortwave radiation, contributing to warming and influencing cloud formation as a CCN (Moteki, 2023; Koch and Del Genio, 2010). Mineral dust, however, exhibits more complex optical behaviour due to its broad particle size distribution (PSD), spanning from fine to super-coarse modes, and variable refractive index, which depends on mineralogical composition (Di Biagio et al., 2017; Ryder et al., 2018). Its extinction efficiency is size-dependent, with studies suggesting that larger particles contribute significantly to the extinction of infrared radiation (Mahowald et al., 2014; Ryder et al., 2019; Fountoulakis et al., 2024). In addition, dust can act as both CCN and INP, affecting cloud microphysics and precipitation processes.

Atmospheric models are important for understanding the dust radiative impact (Kok et al., 2023). However, most model predictions typically include dust particles up to 10 μm, missing a substantial quantity of giant particles and leading to poor representation of the dust load and its radiative effect (Adebiyi and Kok, 2020; O'Sullivan et al., 2020; Drakaki et al., 2022). Given that mineral dust is the most abundant aerosol type by mass, accurately quantifying it and realistically describing its PSD become even more significant.

The quantity and distribution of dust in the atmosphere are among the parameters considered for various environmental and economic applications, including climate projections, air quality assessment, and aviation safety (Middleton, 2017). Remote sensing technologies such as spaceborne lidars (e.g., CALIOP; Winker et al., 2009; ATLID; Illingworth et al., 2015) and ground-based lidar (e.g., EARLINET; Bösenberg and Matthias, 2003, LALINET; Antuña-Marrero et al., 2017, MPLNET; Welton et al., 2001) and sun photometer networks (e.g., AERONET; Holben et al., 1998; SKYNET; Nakajima et al., 2007), provide valuable optical measurements of dust, which when converted into physical quantities like mass concentration, can be utilized in a variety of applications. A key parameter in this conversion process is the volume-to-extinction ratio, which serves a dual purpose: it facilitates the estimation of extinction coefficient from mass concentration, an approach commonly used in atmospheric models (Ghan and Zaveri, 2007), important for assessing radiative effects—and enables the translation of remotely sensed extinction and aerosol optical depth (AOD) into gravimetric quantities, which are useful for most policy formulations.

To achieve this conversion, it is necessary to derive the total volume of dust particles and their extinction, as well as to assume appropriate particle density values. This relationship significantly influences retrieval accuracy, and can be challenging particularly for mixed aerosol types such as desert dust mixed with other aerosols (e.g. pollutants), where this relationship becomes more complex. The extinction coefficient can be derived from observations using sun photometers and lidar, or estimated through atmospheric models. Similarly, the total volume concentration, which is directly related to PSD, can be measured in-situ using optical particle counters (OPCs), retrieved from sun photometer remote sensing observations, or estimated by

https://doi.org/10.5194/egusphere-2025-3404
Preprint. Discussion started: 29 July 2025

models. However, traditional in-situ measurements often provide only ground-level PSDs, which may not be representative of the entire atmospheric column.

Ground-based sun photometers, such as those of the AERONET or SKYNET networks (Holben et al., 1998; Nakajima et al., 2007), offer spectrally resolved AOD and can retrieve fine and coarse mode aerosol properties, including size-resolved volume concentration. When combined with ground-based lidar observations, these measurements enable the inversion of lidar-derived optical properties e.g., Ansmann (2011); Mamouri and Ansmann (2014), allowing for simultaneous retrieval of both columnar and vertically resolved aerosol properties. Sunphotometer-only inversions have inherent limitations, such as the assumption of a single complex refractive index for both fine and coarse particles. Furthermore, AERONET's and SKYNET's retrievals are constrained to a maximum particle radius (15 μm for AERONET, 10 μm for SKYNET v5), which can lead to underestimation of giant particles, as demonstrated by Estellés et al. (2018); Marenco et al. (2018) and Ryder et al. (2018, 2019) for dust events over the Sahara and tropical eastern Atlantic during the Sunphotometer Airborne Validation Experiment in Dust (SAVEX-D) and AERosol Properties – Dust (AER-D) campaigns.

Synergistic algorithms that combine lidar with sunphotometer measurements (e.g. GRASP; Lopatin et al., 2021), overcome some of these limitations, but they are not used operationally as of yet (Tsekeri et al., 2023). Airborne-based observations acquired from in-situ sensors on board aircraft or Unmanned Aerial Vehicles (UAVs) can provide high vertical-resolution profiles of aerosol properties for fine, coarse and giant particles (Haywood et al., 2003; Turnbull et al., 2012; Johnson et al., 2016; Ryder et al., 2015, 2018; Kezoudi et al., 2021a). Airborne in-situ measurements can directly capture PSDs at different altitudes, offering a more detailed view of aerosol distribution that may complement ground-based remote sensing data. These observations are particularly valuable for validating and refining retrieval methods using lidar and/or sun photometer observations.

The Unmanned Research Laboratory (USRL) (Kezoudi et al., 2021a) of the Cyprus Institute provides UAV-related infrastructure and a unique capability for conducting synergistic atmospheric observations using miniaturized and conventional sensors. This mobile facility can perform flights at any chosen location of interest upon authorization, but can also operate from the private runway. The private runway is strategically located near the Cyprus Atmospheric Observatory (CAO) in Agia Marina Xyliatou, which is equipped with ground-based remote sensing observations.

This study explores the volume-to-extinction ratio of mineral dust using the extinction coefficient derived from lidar measurements, and the PSDs measured in-situ with UAVs. During the Fall Campaign 2021 in Cyprus and the ASKOS Campaign 2022 in Cabo Verde, synergistic measurements were conducted using UAV-mounted in-situ sensors, lidar, and sun photometers during dust episodes. These observations provide a unique dataset for deriving volume-to-extinction ratios across different aerosol conditions, including Saharan, Middle Eastern, and mixed dust cases. The retrieved ratios are compared with MOPSMAP scattering calculations (Gasteiger and Wiegner, 2018a) for different refractive indices and shape assumptions (i.e. aspect ratios) to link observations to the theory. Additionally, a comparison between the observed ζ and the predefined ζ used in the WRF-Chem model input is conducted to evaluate how well the model's predefined values represent the aerosol load. The findings of this study contribute to improved aerosol characterization and enhancement of the reliability of remote sensing-based aerosol mass retrievals.

2 Particle microphysical and optical properties, and the volume-to-extinction ratio

Aerosol “quantity” in the atmosphere is often expressed in terms of mass concentration (for example in units of μg/m^3) or by extensive optical properties, e.g. the extinction coefficient (e.g. in units of Mm^{-1}). When the column-integrated quantities are given, the equivalent formulations will be the mass loading (e.g. in g m^{-2}) and the AOD (unitless). Mass is the natural way to express the quantity of matter, and it can be directly obtained at the Earth’s surface from gravimetric measurements or calculated from observations of the particle size distribution. The extinction and AOD are parameters that affect the aerosol direct radiative impact. Moreover, these quantities can be observed by remote sensing through lidar, sunphotometer networks such as AERONET and SKYNET, or passive satellite imagers. The relationship between the gravimetric and the optical properties of aerosols is essential when using optical observations for the validation, tuning and data assimilation for models that represent the aerosols in terms of concentration, and vice versa when using remote sensing observations to estimate gravimetric concentrations.

The conversion factor for extinction-to-mass is called the "specific extinction" (Haywood et al., 2003; Marenco et al., 2011; Johnson et al., 2012). This section outilines the theoretical concept that relates aerosol concentration and the aerosol extinction to the particle microphysical properties, in order to better understand how these influence specific extinction. The specific extinction depends on two terms: the volume-to-extinction ratio (the focus of this article) and the density ρ (not investigated here).

For spherical particles, given a number size distribution $n(r)$, the total aerosol concentration (mass per unit volume) can be expressed as shown in Eq. 1:

$$M = \rho V = \frac{4\pi\rho}{3} \int_0^\infty r^3 n(r)\, dr, \tag{1}$$

where ρ is the density of the particles, V is the total particle volume per unit volume of air, r is the radius of the particles assumed to be spherical, and $n(r)$ is the particle number size distribution function, describing the number of particles per volume and unit radius interval. The aerosol extinction coefficient α, representing the scattering and absorption per unit volume, is expressed as shown in Eq. 2:

$$\alpha = \overline{q_{\mathrm{ext},s}}\ \pi \int_0^\infty r^2 n(r)\, dr. \tag{2}$$

Here, $\overline{q_{\mathrm{ext},s}}$ is the mean extinction efficiency for spherical particles (underscript $_s$) weighted by surface area. It can be expressed as follows:

$$\overline{q_{\mathrm{ext},s}} = \frac{\int_0^\infty q_{\mathrm{ext}}(r) r^2 n(r)\, dr}{\int_0^\infty r^2 n(r)\, dr}, \tag{3}$$

where $q_{\mathrm{ext}}(r)$ is the extinction efficiency for spherical particles of radius r, as computed with Mie theory (Lorenz, 1890; Mie, 1908; Van de Hulst, 1957). It is important to note that the extinction efficiency is dependent upon the refractive index and the ratio between the particle circumference and the wavelength of light (i.e. the size parameter). For spheres, it is typically

https://doi.org/10.5194/egusphere-2025-3404
Preprint. Discussion started: 29 July 2025

between 0 and 5, and it has a typical oscillatory behaviour with particle size, tending to 2 in the geometrical optics limit (large particles compared to the wavelength). By combining Eq. 1 and 2, the specific extinction is expressed as the ratio between α and M:

$$K_{\text{ext}} = \frac{\alpha}{M} = \frac{1}{\rho\zeta}, \tag{4}$$

where ζ is the volume-to-extinction ratio, the focus of this article, has units of length, and can be expressed as follows:

$$\zeta = \frac{V}{\alpha} = \frac{4}{3}\frac{r_{\text{eff},s}}{q_{\text{ext},s}}. \tag{5}$$

In Eq. 5 $r_{\text{eff},s}$ is the effective radius, i.e. the ratio between the third and the second moments of the PSD:

$$r_{\text{eff},s} = \frac{\int_0^\infty r^3 n(r)\,dr}{\int_0^\infty r^2 n(r)\,dr}. \tag{6}$$

For non-spherical particles, the definitions of r_{eff} and $\overline{q_{\text{ext}}}$ can be in general reformulated to:

$$r_{\text{eff}} = \frac{3V}{4A} = \frac{3\int_0^\infty V_p(r)\,n(r)\,dr}{4\int_0^\infty A_p(r)\,n(r)\,dr} \tag{7}$$

and

$$\overline{q_{\text{ext}}} = \frac{\int_0^\infty q_{\text{ext}}(r)\,A_p(r)\,n(r)\,dr}{\int_0^\infty A_p(r)\,n(r)\,dr}, \tag{8}$$

following Schumann et al. (2011), where $V_p(r)$ and $A_p(r)$ are the particle volume and particle projected area, respectively, averaged over different particle orientations, $q_{\text{ext}}(r)$ is the ratio between the cross-section and the projected area of the particle, and r is a measure of the particle size. The factor $\frac{3}{4}$ ensures consistency with equation (6) for spherical particles. Several definitions are possible for r as outlined in Schumann et al. (2011) (e.g. the maximum dimension): amongst those, Gasteiger et al. (2011) retains the projected-area equivalent radius r_c (also called the geometric cross-section-equivalent radius) and the volume-equivalent radius r_v. Following the latter paper's equation (11) expression for ζ can be formulated using an additional parameter Ψ, the sphericity:

$$\zeta = \frac{4}{3}\frac{\Psi \cdot r_{\text{eff}}}{\overline{q_{\text{ext}}}}, \tag{9}$$

with Ψ defined as

$$\Psi = \frac{3\sqrt{\pi}}{4}\frac{V_p}{A_p^{3/2}} \tag{10}$$

For particles that are not spherical, $\Psi < 1$, whereas $\Psi = 1$ is in the case of spheres (consistent with the general concept introduced by Wadell, 1935).

The volume-to-extinction ratio is a measure of how the volume of particles relates to their extinction properties, and it is important for understanding how particle size affects the overall optical properties of aerosol populations. From Eq.9, it becomes evident that an increase in r_{eff} in the Mie and geometric optics regime, leads to an increase in the volume-to-extinction ratio, assuming other factors (such as the extinction efficiency) remain constant. Figure 1 illustrates the relation described in eq 9 for the refractive indices of water, mineral dust and black carbon in the case of different sphericities, at 532nm. The particle number distribution $n(r)$ used here is based on Eq. 17 for $n_0 = 100$, $\sigma = 1.5$ and r_0 ranging between $0.01 \mu m$ and 100 μm.

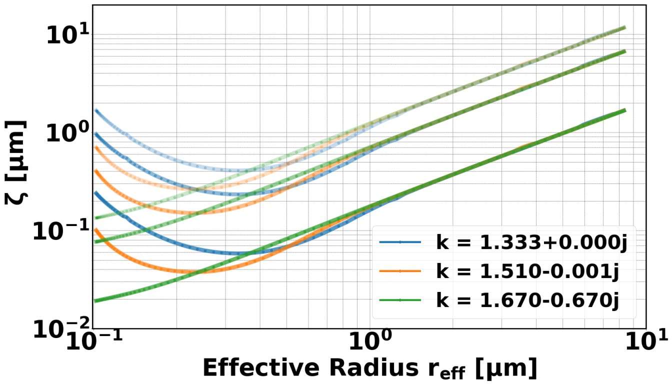

Figure 1. Theoretical relation between volume-to-extinction ratio (ζ) and effective radius (r_{eff}) at 532 nm, for a selected range of refractive indices (k): water (blue), dust (orange) and black carbon (green) (as in Seinfeld et al., 2006, Di Biagio et al., 2019 and Zhao et al., 2020). Transparency is changing for changing sphericity Ψ = (0.1,0.4,0.7,1) with more intense colour being $\Psi = 1$.

From the plot, it is evident that the relation is not linear but there is an increase in ζ with increasing effective radius, except for small effective radii.

When considering larger particles where $\frac{2\pi r}{\lambda} \gg 1$ Eq. 9 is simplified as in geometric optics $\overline{q_{\text{ext}}} \simeq 2$ and ζ becomes:

$$\zeta = \frac{V}{\alpha} \simeq \frac{2}{3} \cdot \Psi \cdot r_{\text{eff}}. \tag{11}$$

For larger particles, their volume increases more than their ability to scatter and absorb light, and thus the volume-extinction ratio also increases. In the geometric optics regime the relation between ζ and r_{eff} is linear. In this study, the instruments observed particles with radii ranging from 0.06 to 30 μm, covering a range that includes both the Mie scattering and geometric optics regimes, considering a wavelength at 532 nm.

3 Observational datasets and models

3.1 Campaigns

3.1.1 Fall Campaign

The Cyprus Fall Campaign 2021, conducted from October 18 to November 18 2021, in Orounda, Cyprus, aimed to investigate the microphysical properties of mineral dust transported over Cyprus through airborne in-situ and ground-based remote sensing observations. Using UAVs equipped with OPC instruments, in situ particle measurements were conducted, capturing a wide range of particle sizes. The UAVs also carried the Compact Optical Backscatter Aerosol Detectors (COBALDs, data not utilized in this paper) and the Giant Particle Collector (GPaC), a miniaturized body impactor designed for UAVs to collect super-micron particles. Data acquired during these flights allowed to calculate total number concentration and volume size distributions. In addition to these airborne in-situ observations, ground-based remote sensing measurements were conducted at the Cyprus Atmospheric Observatory (CAO, https://cao.cyi.ac.cy/, last access: 25th June 2025) of the Cyprus Institute (CYI) in Nicosia (CAO-NIC) and Agia Marina Xyliatou (CAO-AMX). These included a dual-wavelength polarization lidar (CE376) capable of detecting altitudes up to 18 km, and sun-photometers (CE318, CE318T) for measuring columnar aerosol properties like AOD and Ångström exponent. Together, the airborne and remote sensing measurements provided valuable insights into the vertical distribution and optical properties of dust transported to Cyprus.

3.1.2 ASKOS Campaign

ASKOS (Marinou et al., 2023), the ground-based component of the Joint Aeolus Tropical Atlantic Campaign (JATAC) organized by the European Space Agency (ESA) and the National Aeronautics and Space Administration (NASA) in 2021-2022, took place in São Vicente, Cabo Verde, to provide reference measurements for calibrating and validating the aerosol products of the Aeolus satellite mission (Fehr et al., 2023). Additional scientific objectives were to study possible dust orientation in the atmosphere (Tsekeri et al., 2025, in preparation), quantify the dust interactions with water vapour, investigate the mixing and transport of giant particles in the Saharan air layer and boundary layer, characterise cloud microphysics in the Eastern Atlantic, and analyse the impact of dust particles on cloud formation and radiation. ASKOS utilized advanced instruments such as the multi-wavelength Raman polarization-water vapour lidar Polly^{XT} (Engelmann et al., 2016; Baars et al., 2016), the AERONET sun-photometer, the scanning Doppler wind lidar (HALO), the microwave radiometer, and the 94 GHz cloud radar (FRM4Radar). Aeolus aerosol product Cal/Val was performed with the ESA reference lidar eVe (Paschou et al., 2021). Reference atmospheric electricity sensors, radiosondes and radiation measurements were also deployed. Part of the ASKOS/JATAC campaign was the CYI airborne campaign between 08-30 June 2022, with the deployment of airborne in-situ measurements from OPCs on board UAVs, enriching the dataset for aerosol characterization. Similar to the Fall Campaign 2021, the COBALD and the impactors were also carried by the UAVs.

3.2 Remote sensing observations

3.2.1 CIMEL CE376 Lidar

The CIMEL CE376 is a compact elastic backscatter lidar developed by CIMEL in France. It is a dual-wavelength polarization lidar (Papetta et al., 2024) equipped with a laser diode and a frequency-doubled Nd:YAG laser, operating in the near-infrared (808 nm) and green (532 nm) with a repetition rate of 4.7 kHz. It measures backscatter signals in three detection channels, one for the infrared and two for green, co-polar and cross-polar channels. For all the reception channels, the lidar uses photon-counting acquisition through avalanche photodiode detectors (SPCM-AQRH modules from Excelitas). The system has continuous day and night operations with a typical maximum detection altitude of around 10 km for the day and 18 km for the night. The signal is recorded in 2048 successive bins spaced by 15m in the vertical direction from 100 m up to a range of 30 km.

The CIMEL lidar was installed in September 2021 at CAO-Nicosia, Cyprus and has been running continuously since. This lidar is part of the ICARE network: Cloud-Aerosol-Water-Radiation Interactions network (ICARE, https://dataviz.icare.univ-lille.fr/lidar_panel/, last access: 25th June 2025).

3.2.2 Polly^{XT} Lidar

Polly^{XT} is a transportable aerosol multiwavelength Raman and polarization lidar type designed for continuous profiling of the atmosphere. The instrument setup has steadily improved from single-wavelength systems (Althausen et al., 2009) to multi-wavelength lidars with near-range and water vapor profiling capabilities (Engelmann et al., 2016). The Polly^{XT} deployed at Mindelo Cabo Verde has the capability to measure particle backscatter and extinction coefficients (with Raman method), and particle depolarization ratio at all three emitted wavelengths of 355 nm, 532 nm, 1064 nm (Gebauer et al., 2024). Furthermore, it has a near-range receiver in the UV and the visible wavelengths (elastic and raman) and water vapor profiling capabilities (407 nm). Additionally, the dual–field-of-view methodology has been implemented (Jimenez et al., 2020). The depolarization channels enable the differentiation between spherical and non-spherical aerosol particles through particle depolarization ratio (PDR) measurements. Various studies demonstrated Polly^{XT}s potential for aerosol monitoring in Central Asia (Hofer et al., 2017, 2020a, b) and southernmost South America (Jimenez et al., 2020).

In July 2021, the Polly^{XT} lidar system was deployed in Mindelo, Cabo Verde, as part of the ASKOS campaign (Marinou et al., 2023), and it has been operating continuously since its installation, becoming a permanent installation. Also, this Polly^{XT} is part of PollyNET, a network comprising both permanent and campaign-based Polly lidar stations (Baars et al., 2016).

3.2.3 Sunphotometer

Sun- and sky-scanning spectral radiometers from the AErosol RObotic NETwork (AERONET; Holben et al.1998) were co-located with the lidars during both campaigns to collect observations of aerosol properties. AOD, which represents the column-integrated aerosol extinction coefficient and the Ångström exponent are calculated from direct sun measurements. In addition, the sunphotometers collect sky radiance measurements in the almucantar geometry, allowing for the retrieval of a large suite of microphysical and optical properties of aerosol particles, such as volume size distributions and single scattering albedo (Dubovik and King, 2000). The instruments measure across eight spectral bands, ranging from 340 nm to 1020 nm.

In the Fall Campaign of 2021 in Cyprus, a lunar/sun-sky photometer (CE318T) was colocated with the lidar at CAO-Nicosia, while another photometer (CE318) was deployed at CAO-AMX, a remote site unaffected by urban pollution near the airfield of UAV operations. The sunphotometer in Nicosia was used to constrain the lidar ratio for the retrievals of the extinction and backscatter coefficients (Klett, 1985; Fernald, 1984). The size distributions reported in this paper are derived from the CAO-AMX sunphotometer. During the ASKOS campaign in Cabo Verde, a lunar/sun-sky photometer (CE318T), was employed for observations in Mindelo.

3.3 UAV based observations

The Unmanned Systems Research Laboratory (USRL, https://usrl.cyi.ac.cy/, last access: 25th June 2025) is part of CARE-C of the Cyprus Institute and offers on-site facilities and related infrastructure for research, development, and testing of technologies related to UAVs (Unmanned Aerial Vehicles). USRL owns a private airfield at Orounda [N35°5′42.18″, E33°4′54.19″], 327 m above sea level (a.s.l.), with a clear view of the northwestern side of the island (19 km distance from the sea). The airfield's location is strategically selected to be near the CAO-AMX station. UAV-based sensors provided by third parties are employed on board the UAVs. The sensors used in this study are described in the following subsections.

3.3.1 POPS

The Portable Optical Particle Spectrometer (POPS), developed at the NOAA Chemical Sciences Laboratory, is a lightweight OPC (0.8 kg without battery) designed to be deployed as a balloon-borne instrument or on board UAVs. POPS has a 405-nm diode laser and can measure aerosol number concentration in the diameter range from 0.14 to 3.0μm. A dryer is inserted at the inlet of the instrument to dry the aerosols and prevent any damage, especially when the UAV-POPS system flies inside humid environments (Gao et al., 2016). Comparisons with reference ground and UAV-based observations showed that POPS can provide reliable vertical profiles of particle size distribution (Mei et al., 2020). The sampling volume of POPS is based on the sampling flow, which is approximately 3 cm^3/s.

3.3.2 UCASS

The Universal Cloud and Aerosol Sounding System (UCASS) developed by the University of Hertfordshire, is a lightweight OPC (∼230 g) designed for use as a balloon-borne instrument, as a dropsonde, or on board UAVs (Smith et al., 2019). The UCASS operates a 658 nm laser diode. Depending on the configuration mode and the laboratory calibration, UCASS can measure dust in the radius (optical) range between 0.2 and 39.0 μm. Previous studies showed that UCASS airborne particle size distributions and number concentrations were in close agreement with other reference airborne OPCs, e.g. the Cloud, Aerosol, and Precipitation Spectrometer (CAPS, Kezoudi et al.,2021b). During the ASKOS campaign, two UCASS units were mounted on a fixed-wing UAV, one under each wing. The first UCASS covered a size range of 0.3–15 μm for dust particles, while the second spanned 2–39 μm. In the Fall Campaign, two UCASS units were mounted on the wings, with a size range of 0.3–20 μm for both. In this paper, data from both UCASS units are combined. The sampled air volume in UCASS is specified as $v = Ax$ with a sample area of $A = 5.0 \times 10^{-7} m^2$ and $x = ut$ the distance covered by the UAV with a known airspeed u m/s during a time t.

3.3.3 Impactors

A miniaturized and 3D-printed version of the Giant Particle Collector (GPaC, Lieke et al. 2011), a body impactor, designed for UAV applications, was also deployed under the wings. The modified GPaC collects particles sized up to several hundred micrometers, with the lowest cut-off ranging between 1 and 5 μm, depending on air speed, pressure, and temperature. An adhesive carbon substrate is affixed to a 1.1 cm diameter impactor head, which is inserted into a holder on the UAV and exposed during selected sections of a flight, sampling interesting aerosol layers (e.g., a dust layer). The impactors are analyzed offline using Scanning Electron Microscope analysis, which provides information on particle size, aspect ratio, refractive index, morphology, and the chemical and mineralogical composition of each sample (Kandler et al., 2009, 2018). During the Fall and ASKOS campaigns, two GPaC samplers were employed on board the UAV—one on each wing—and were set to open at specific altitude ranges. This paper utilizes the aspect ratios and refractive indices from the samples.

3.3.4 Meteorological parameters

Relative humidity (RH) and air temperature (T) data are recorded during UAV flights. These measurements are obtained with the HC2-ROPCB sensor (from the Rotronic Company) mounted below the aircraft's wing. A customized 3-D printed probe houses the sensor to protect it from possible shocks and direct solar irradiance while ensuring proper air flow during flight (Kezoudi et al., 2021a).

3.4 MOPSMAP model

The MOPSMAP algorithm by Gasteiger and Wiegner (2018b) (Modeled Optical Properties of Ensembles of Aerosol Particles), based on Fortran, offers a computationally efficient approach for optical modeling with complex aerosol shapes. MOPSMAP considers optical properties of spheres as well as spheroids (prolate or oblate with $1 \leq \mathrm{AR} \leq 5$) and irregular particle shapes in random orientation over a range of sizes and refractive indices. This paper utilizes the MOPSMAP web interface to calculate the optical properties of dust by using as input the wavelength (one lidar wavelength in this case), refractive indices (based on impactors and AERONET), shapes (spheroids and spheres), and sizes based on the OPC observations of the PSDs. Note that

3.5 WRF-Chem model

The Weather Research and Forecasting regional atmospheric model coupled with chemistry (WRF-Chem) is a fully integrated meteorology-chemistry-aerosol model developed through a collaborative effort led by NOAA/ESRL. WRF-Chem simulates

https://doi.org/10.5194/egusphere-2025-3404
Preprint. Discussion started: 29 July 2025

the emission, transport, deposition, mixing, and chemical transformation of trace gases and aerosols, as well as aerosol interactions, photolysis, and their interactions with meteorology (Grell et al., 2005). Additionally, cloud chemistry, aerosol-cloud interactions, and their feedback processes are incorporated into the model (Fast et al., 2006; Chapman et al., 2009).

This study makes use of the Georgia Tech/Goddard Global Ozone Chemistry Aerosol Radiation and Transport (GOCART) dust emission scheme to get the simulated emission, transport and deposition of the dust over the sites of interest. GOCART uses five particle sizes from 0.1 to 10μm (radius). Aerosol optical properties are calculated using a parameterized Mie theory (Ghan and Zaveri, 2007), adapted for a size-resolved size distribution (Fast et al., 2006; Barnard et al., 2010). Two different setups are used in this study to cover the Cyprus and Cabo Verde cases. The first setup, operated by the CyI, has a model domain extending from 7 ° N to 57 ° N and from 28 ° W to 78 ° E, with a horizontal resolution of 20 km. It also includes the main sources of dust in the Middle East and North Africa. The second setup, operated by NOA, covers a domain bounded between 1.42 ° N and 39.99 ° N and stretches from 30.87 ° W to 46.87 ° E, with a horizontal resolution of 20 km. Both models use 32 vertical pressure levels.

The CYI set-up was tested for 13 different GOCART schemes, testing various combinations of options (manuscript in preparation, Louka E.). These included nudging (applied to constrain meteorological fields), aerosol-radiation feedback (aer_ra_feedback=0 or 1 to toggle feedback), and prognostic dust treatment (progn=0 or 1 to enable or disable dynamic dust evolution). Only one run was used in this manuscript and had the following settings: aer_ra_feedback=1, progn=1 with nudging of a scale parameter = 0.4.

Here, the focus is on the relationship between the extinction coefficient and the mass concentration of coarse soil-derived aerosols. These parameters are used to calculate the modeled volume-to-extinction ratio and compare it with observations.

4 Methodology

4.1 Case selection

From the two campaigns, some cases are selected where observations were available from OPCs on board UAVs, lidar, and sunphotometers. The first criterion for selection was the availability of these multi-instrument datasets, as they are the basis for applying the described methodology. Additionally, the focus is on cloud-free days to ensure reliable extinction retrievals from the lidar and accurate size distribution retrievals from AERONET. A final criterion was to select cases with a significant amount of particles (AOD > 0.2) and large particles (e.g. dust-dominated cases), to ensure that the observations were made during a well-developed dust event. The cases that meet these criteria are presented in Table 1. Back trajectory analysis using the HYSPLIT model (Stein et al., 2015) revealed the origin of the air masses at the dust layer altitude ranges.Only one case from the ASKOS campaign was included, as the combined requirements for cloudless conditions and UAV observations using both POPS and UCASS significantly limited the number of available cases for applying the methodology. Furthermore, in some cases that met these criteria, changes in the aerosol layer formation between the UCASS and POPS flights prevented the observations from being meaningfully combined.

https://doi.org/10.5194/egusphere-2025-3404
Preprint. Discussion started: 29 July 2025

Table 1. Overview of the selected cases during Fall and ASKOS campaigns. Cases marked with (*) are used as demonstration cases in the methodology section. The presented r_{eff} is calculated according to Eq.6.

			UAV based				Lidar		Sunphotometer	
Date	**Campaign**	**Dust Origin**	**POPS takeoff-landing (UTC)**	**UCASS takeoff-landing (UTC)**	**Max climbed alt POPS//UCASS (km ASL)**	**Dust Layer r_{eff} (μm)**	**Dust layer height (km ASL)**	**VLDR**	**AOD NIC//AMX or OSCM**	**Ångstrom 447-870 nm**
25/10/2021	Fall Campaign, Cyprus	Central Sahara	13:09-14:09	14:24-15:30	3.7//4.0	1.29	2.5-5.2	0.13	0.20//0.16	1.174//1.102
27/10/2021	Fall Campaign, Cyprus	Central Sahara	11:42-12:32	10:48-11:36/13:11-13:59	3.9//4.2/4.0	1.50	2.1-4.4	0.13	0.29//0.28	0.768//0.638
14/11/2021	Fall Campaign, Cyprus	Middle East	13:56-14:39	12:30-13:50/14:42-15:35	3.2//4.4/1.8	1.60	1.4-3.5	0.18	0.28//0.24	0.904//0.816
15/11/2021*	Fall Campaign, Cyprus	Middle East	13:46-14:32	12:37-13:33/14:38-15:36	3.2//4.4/1.5	1.58	1.4-3.4	0.17	0.31//0.25	1.013//0.998
18/11/2021	Fall Campaign, Cyprus	Mixed	13:12-13:58	14:21-15:11	3.8//4.5	1.51	1.4-3.1	0.12	0.37//0.34	1.127//1.104
24/06/2022*	ASKOS, Cabo Verde	West Sahara	15:38-16:51	18:18-19:17	4.9//4.9	3.45	1.6-4.3	0.23	0.47	0.115

Two selected case studies are used to demonstrate the methodology: (i) 15th November 2021 from the Fall Campaign in Cyprus and (ii) 24th June 2022 from the ASKOS campaign in Cabo Verde (cases with (*) on Table 1) to examine the application of the method for different dust load and origin. As seen in Table 1, the depolarization, AOD, Ångström, r_{eff} and vertical depth of the two cases differ significantly, with the second case showing higher AOD and VLDR values and extending over a larger vertical depth. The second case observed at Cabo Verde is directly on the path of long-range transported dust over the Atlantic carried by the Saharan Air Layer (SAL), which is related with high-value AOD and can extend up to 5 km (Karyampudi et al., 1999; Prospero et al., 2014; Tsamalis et al., 2013).

4.2 Remote sensing

4.2.1 Lidar observations

Figure 2 shows the 532-nm volume linear depolarization ratio (VLDR) profiles time series for the two demonstration cases. The times of the UAV flights (indicated by the white dashed lines), of the available size distributions from AERONET (black lines), and of the selected lidar profiles (red box) are also shown in the same figure. It should be noted that the lidar profiles selected for analysis correspond to the times closer to the OPC observations and have no clouds in the profile. Comparing the time series of the two cases, the dust layer on 15th November 2021 appears more uniform, extending from the ground up to approximately 3 km. In contrast, the case on 24th June 2022 shows multiple aerosol layers at different altitudes, with the most VLDR-intense layer located between approximately 3–4 km. The cloud-free lidar profiles within the red box were averaged over time to produce one profile seen in Fig. 3.

The Fernald–Klett method (Fernald, 1984; Klett, 1985) was used to derive the aerosol extinction coefficient profiles from the lidar measurements (note that Raman data from Polly^{XT} were not available during the daytime). The retrieval was constrained using sunphotometer AOD measurements, and this constraint was satisfied with a lidar ratio (LR) of 35 sr for 15th November 2021 and 50 sr for 24th June 2022 (Marenco et al., 1997). It should be noted that the choice of LR introduces a source of uncertainty in the lidar retrievals; however, addressing this uncertainty is beyond the scope of the present study.

https://doi.org/10.5194/egusphere-2025-3404
Preprint. Discussion started: 29 July 2025

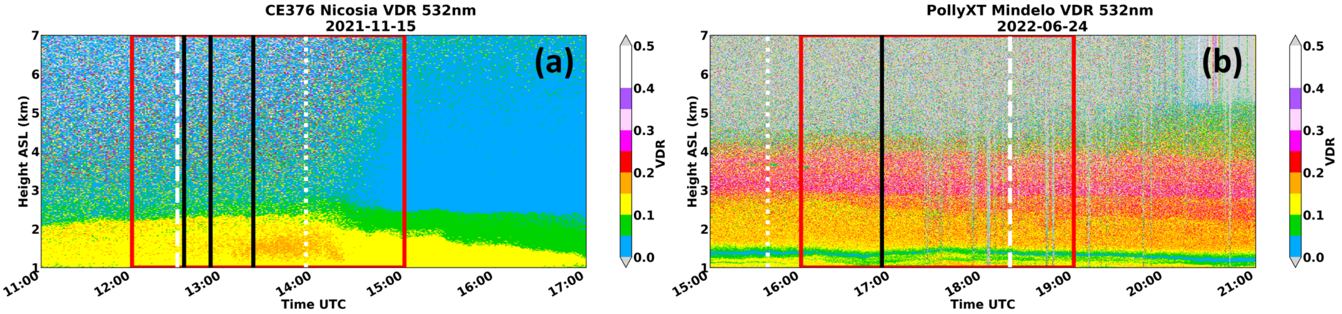

Figure 2. VLDR profiles for 15th November 2021 (a) and 24th June 2022 (b). Vertical lines indicate the timestamps of available PSDs from AERONET (black solid lines), UCASS take-off time (dashed white line), POPS take-off time (dotted white line), and the chosen lidar interval (red box).

335 The extinction coefficient and VLDR profiles for the two cases are shown in Fig. 3, which help confirm the altitudes of the dust layers listed in Table 1. As mentioned before, the 24th June 2022 presents higher extinction coefficients and VLDR for the particles than the 15th November. These extinction profiles are used further in the analysis for the calculations of the ζ parameter. The VLDR is shown here for qualitative purposes (i.e. aerosol typing) but it is not further used in the data analysis.

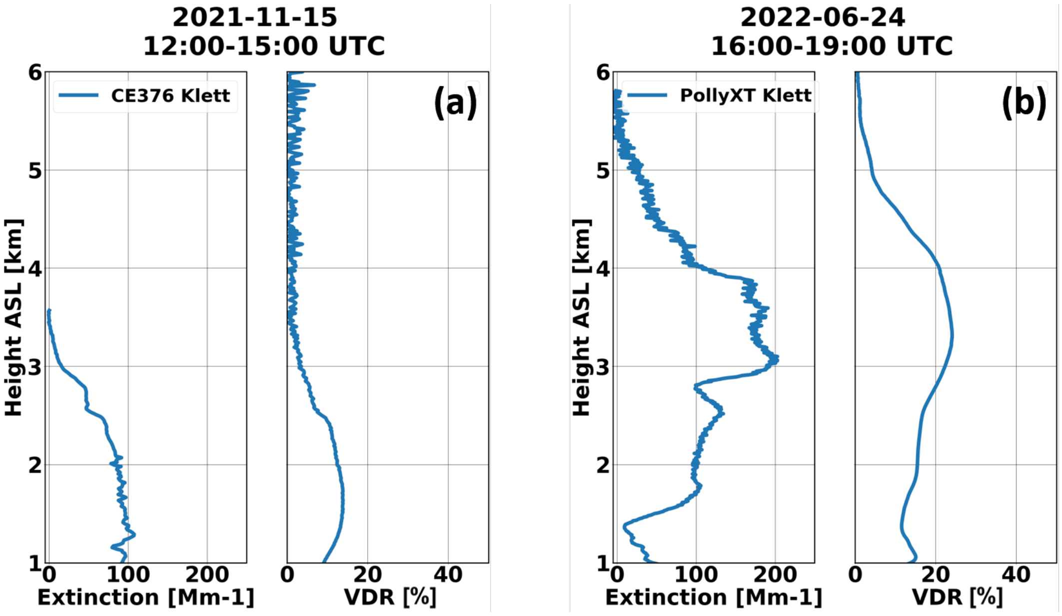

Figure 3. Three-hour averaged extinction coefficient and VLDR profiles for 15th November 2021 (a) and 24th June 2022 (b). The following reference altitudes (z_{ref}) were used for the Klett inversions: (a), z_{ref} = 3.4 km and LR = 35 sr; for (b), z_{ref} = 5.8 km and LR = 50 sr.

4.2.2 AERONET

340 The columnar volume size distribution, $\frac{dV(r)}{d\log r}$ (in $\mu\mathrm{m}^3/\mu\mathrm{m}^2$), where "log" refers to the natural logarithm (as throughout the remainder of this paper), is retrieved from AERONET at 22 logarithmically equidistant discrete points, denoted as r_i for radius, within the size range $0.05\,\mu\mathrm{m} \le r_i \le 15\,\mu\mathrm{m}$. To ensure higher retrieval accuracy, only PSDs with a sky error of less than 5% are included in this analysis (to ensure low discrepancy between measured and model-fitted sky radiances). Figure 4 provides an example of the column-averaged PSDs from the two demonstration cases used. The PSD from November 15, 2021, exhibits 345 a more balanced contribution of fine and coarse modes, whereas the PSD from June 24, 2022, is dominated by coarse-mode particles, which, considering also the lidar observations, are non-spherical dominated.

When multiple size distributions are available within the time interval considered, an average distribution is computed and used in the analysis to reduce variability and enhance data reliability.

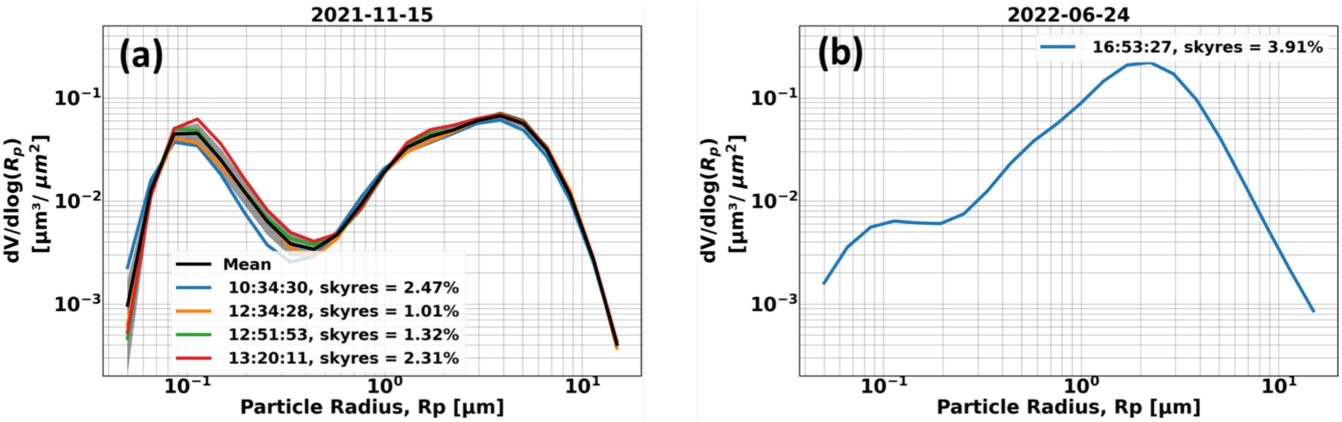

Figure 4. AERONET column-averaged volume size distributions (colored lines) for 15th November 2021 (a) and 24th June 2022 (b). The average size distribution (black line) and its standard deviation (grey shaded area) are shown for the case with more than one size distribution in the considered time interval.

4.3 OPC observations

350 The first step when using the OPC observations is the data filtering. First, cloud screening is applied by discarding all observations for which the relative humidity exceeds 90% and the particle counts per second at each bin are above a threshold given by the manufacturer (UCASS: 1000 counts/s and POPS: 5000 counts/s). Additionally, to ensure optimal particle sampling for UCASS, only observations when the aircraft flew at an airspeed between 4 and 16 m/s are accepted. The values not passing these criteria are omitted.

355 Figure 5 shows temperature and relative humidity profiles during the UAV flights on November 15, 2021 and June 24, 2022. Red and yellow points represent data filtered based on the humidity and airspeed criteria, respectively, as outlined above. In one case, the main reason for excluding data was the airspeed being outside the acceptable range (November 15, 2021), while

in the other, it was due to high humidity (June 24, 2022). In both cases, the filtered data points were less than 20% of the total data.

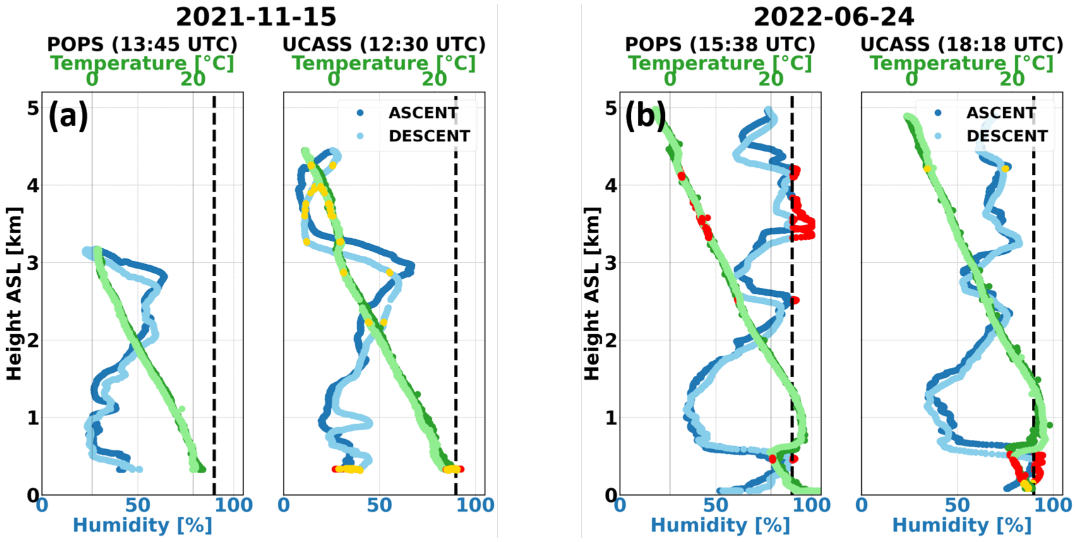

Figure 5. Temperature (green) and humidity (blue) profiles measured during the UAV flights on 15th November 2021 (a) and 24th June 2022 (b) during ascent (dark blue and green) and descent (light blue and green). Red marked points indicate the discarded observations due to the RH criterion (<90%) and the yellow points the discarded observations due to the airspeed threshold (>4, <16 m/s). The dashed line marks the 90% humidity threshold.

360 4.3.1 Concentration calculations and PSD

The next step is to calculate the number concentration profiles from the count measurements of the two OPCs. To ensure consistency between the sensors, the observations are resampled into 10-meter deep layers, providing uniform profile resolution. The ascent and descent profiles for each OPC (POPS, UCASS-1 and UCASS-2) are combined by calculating the average of the two profiles each 10-m segment. The particle concentration (N_{c_i}) at a given altitude z and each size bin of radius r is then 365 calculated using the following equation:

$$N_{c_i}(z) = \frac{\text{counts}_{z,i}}{\text{vol}} \tag{12}$$

where $\text{counts}_{z,i}$ represents the count of particles within the i^{th} bin and vol is the sampling volume of the instrument at altitude z. The sampling volume varies for each instrument, with distinct values for POPS and UCASS as described in Sections 3.3.1 and 3.3.2. The total concentration at each altitude can then be calculated by summing up all the bins as:

370 $$N_c(z) = \sum_{i=0}^{k} N_{c_i}(z) \tag{13}$$

Figure 6 illustrates the total concentration profiles averaged between ascent and descent for the two case studies (15th November 2021 and 24th June 2022), with the standard deviation shown with the shaded regions. The concentration profiles follow the same trend as the extinction coefficient profiles shown in Fig. 3.

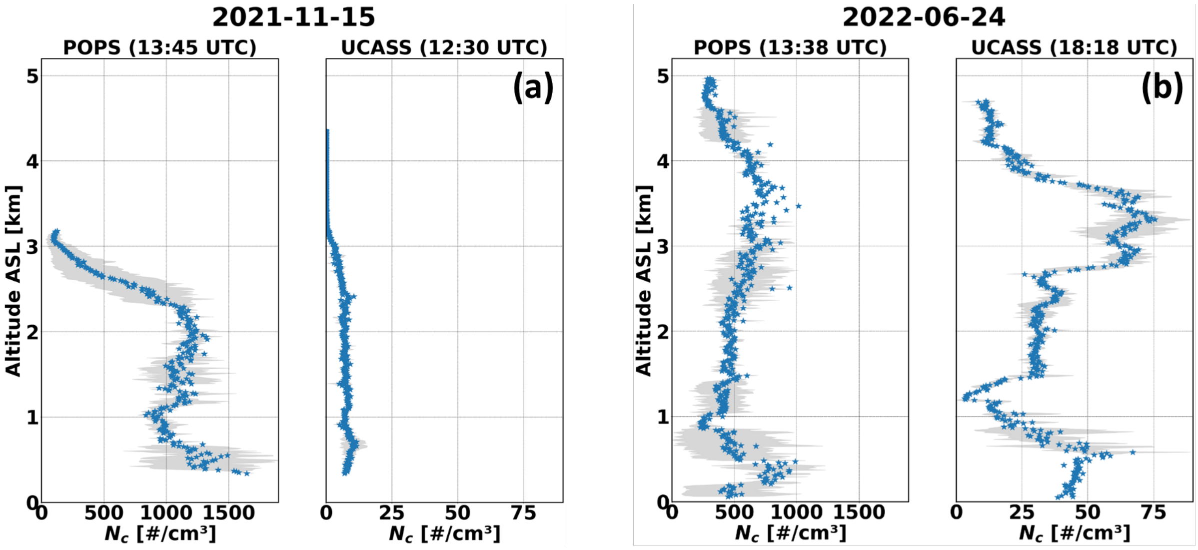

Figure 6. Number concentration profiles for 15th November 2021 (a) and 24th June 2022 (b). The grey shaded area indicates the standard deviation in concentration between ascent and descent profiles.

Using the number concentration $N_{c_i}(z)$, the particle volume size distribution (PSD) can be expressed as follows:

375 $$V(r_i,z) = \frac{4\pi}{3} r_i^3 \cdot N_{c_i}(z) \tag{14}$$

The volume-weighted distribution $\frac{dV(r_i,z)}{d\log(r_i)}$ can be calculated by scaling $N_{c_i}(r,z)$ by $d\log(r_i)$ that represents the logarithmic bin width. Figure 7 shows the volume and number particle size distributions for the two case studies, for different altitude ranges. Data from POPS and UCASS are plotted as circles and triangles, respectively.

The PSDs differ significantly between the two cases. On 15th November 2021, both fine and coarse modes are pronounced as was seen also in Fig. 4, with concentrations having less coarse particles above 2.5 km. In contrast, the volume PSDs on 24th June 2022 are dominated by the coarse mode fraction, with minimal contribution from finer particles. Interestingly, for this case, particles with radii larger than 10 μm are observed by the OPCs up to 4 km above ground level. This giant mode contribution was observed during previous airborne campaigns, including SAVEX-D in Cabo Verde (Ryder et al., 2018).

To create a comprehensive PSD, measurements from the three sensors (POPS and 2 UCASS) are combined by merging all size bins and fitting a lognormal distribution.

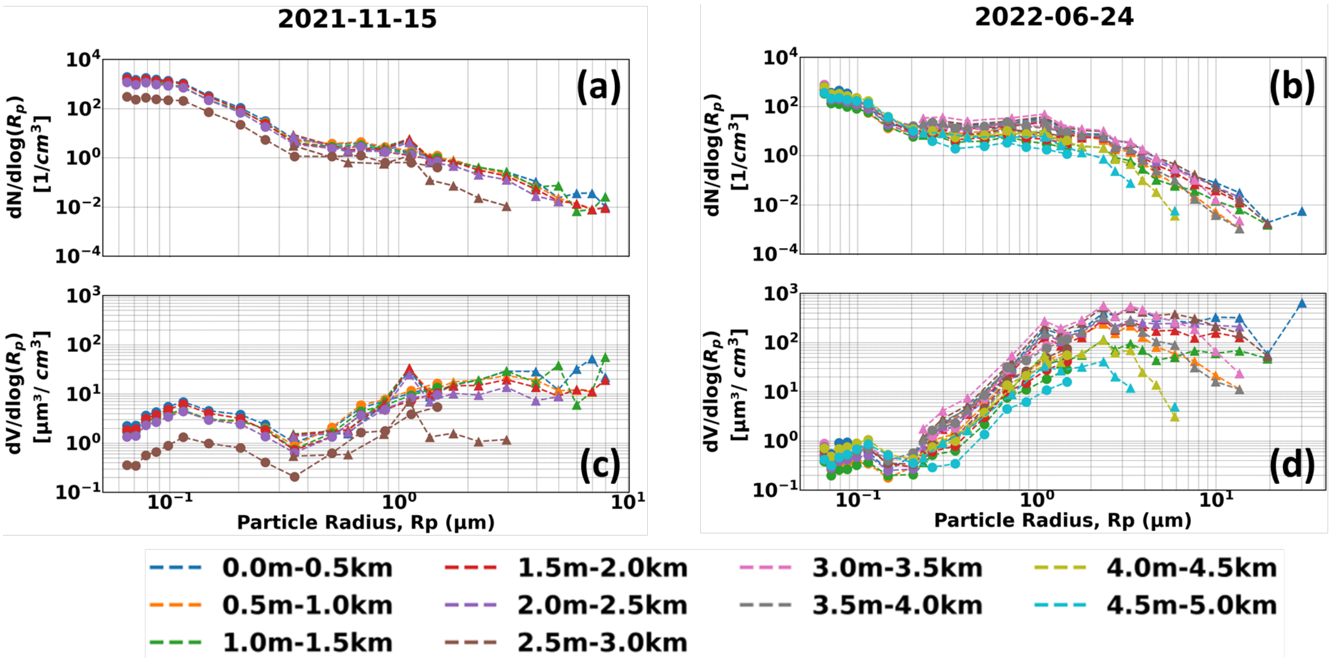

Figure 7. Volume and number particle size distributions for 15th November 2021 (a,c) and 24th June 2022 (b,d) at different altitudes from ground level. Circle points indicate the measurements by POPS, whilst triangles are the measurements from UCASS. The maximum altitude reached by the UAV was 3 km and 4.5 km a.g.l. on 15th November 2021 and 24th June 2022, respectively.

4.3.2 Uncertainties associated with OPC observations

The uncertainty of OPC observations includes two components: statistical (counting) uncertainty and uncertainty in the estimation of the sample volume.

Statistical uncertainty arises from the number of particles counted during a given sampling period. It depends on both the sampling duration and the particle number concentration in each size bin and can be described using Poisson statistics: $\delta N = \sqrt{N}$.

For open-path instruments such as UCASS, the sample volume is estimated as $vol = Avt$, where A is the sampling area ($A = 50 \times 10^{-7}\,\mathrm{m}^2$), v is the aircraft speed (typically 10–12 m/s, measured via pitot tube), and t is the sampling time. The relative uncertainty in particle number concentration is then given by:

$$\frac{\delta N_c}{N_c}_{UCASS} = \sqrt{\left(\frac{1}{\sqrt{\text{counts}}}\right)^2 + \left(\frac{\delta A}{A}\right)^2 + \left(\frac{\delta v}{v}\right)^2} \tag{15}$$

where $\frac{\delta A}{A}$ and $\frac{\delta v}{v}$ represent relative uncertainties in area and speed, which are approximately $\sim 2\%$ and $\sim 5\%$ respectively.

For POPS, the sample volume is determined by the flow rate of the internal pump: $vol = Qt$, where the flow rate Q is approximately 2.9 cm^3/s, as recorded by the instrument. This flow is monitored using a laminar flow element (LFE) and a differential pressure (DP) sensor. The LFE-DP system has an associated uncertainty of approximately 5% (Gao et al., 2016). Considering these, the relative uncertainty of particle number concentration for POPS is:

$$\frac{\delta N_c}{N_c}_{POPS} = \sqrt{\left(\frac{1}{\sqrt{\text{counts}}}\right)^2 + \left(\frac{\delta Q}{Q}\right)^2} \tag{16}$$

Considering eq. 15 and 16 for counts=10, the relative uncertainties are dominated by the statistical components and are in both cases $\sim 32\%$. From the equations, it is obvious that the relative uncertainties will approach a minimum value ($\sim 5\%$) as the number of counts approaches infinity.

An additional source of uncertainty for both UCASS and POPS is related to the particle diameter corresponding to each bin, which depends on the optical properties of the particles. This study relies on manufacturer-provided calibrations for the two instruments (Smith et al., 2019; Gao et al., 2016). Particle sizing also depends on the refractive index of the aerosols: UCASS calibration for dust RI ($m = 1.52 + 0.002i$) is provided by the manufacturer, while POPS is calibrated using polystyrene latex (PSL) spheres and dioctyl sebacate (DOS), with refractive indices of $m = 1.615 + 0.001i$ for PSLs and $m = 1.45 + 0i$ for DOS (Gao et al., 2016). In order to correct for the RI in the case of POPS, Mie scattering calculations are performed, and the correction is $\sim 4\%$ on the diameter for dust RI ($m = 1.52 + 0.002i$). For POPS size bins below 1.22 μm, this results in a diameter correction of less than 0.05 μm, and up to 0.1 μm for bins above 1.22 μm. Given the small magnitude of this correction and its impact on the volume concentration, it is not applied to the POPS data and can be considered negligible.

4.3.3 Log-Normal fits

Lognormal fits are widely used as they tend to provide the best representation for most airborne particle size distributions and smooth out sensor noise. Their simplicity and ability to combine various modes to describe PSDs shapes make them a standard choice in aerosol research and related fields (Pöhlker et al., 2023; Boucher, 2015; Kulmala et al., 2012). The lognormal distribution is characterized by the geometric mean radius R_g and the geometric standard deviation σ, which allow for the representation of both single-modal and multi-modal size distributions (Heintzenberg, 1994).

In this study, a bi-modal lognormal fit is applied to describe the PSDs. Using two lognormal modes, the observations of the chosen flight dates (Table 1) were fitted at 500 m averaged vertical layers.

For a multi-modal distribution, with coarse and fine modes, the following lognormal model is used:

$$\frac{dN}{d\log R_p} = \sum_{i=1}^{n} \frac{N_i}{\sqrt{2\pi}\log\sigma_i} \exp\left(-\frac{(\log R_p - \log R_{g,i})^2}{2(\log\sigma_i)^2}\right) \tag{17}$$

where N_i is the total number concentration of particles, of mode i, $R_{g,i}$ is the geometric mean radius of the mode, and σ_i is the geometric standard deviation of the mode.

The fitting process accounted for all the data from the two UCASS and the POPS instruments to provide a combined smoothed range PSD as shown in Fig. 8 (a,c) and (b,d), representing measurements taken on November 15, 2021, and June 24, 2022, respectively, for 1.5-2 km and 2-2.5 km range. In these two examples, a 2-mode lognormal was fitted to the data, with corresponding R_g and σ provided in the legends of the plots. The resulting lognormal curves provide the best fit to the data according to the calculated standard errors.

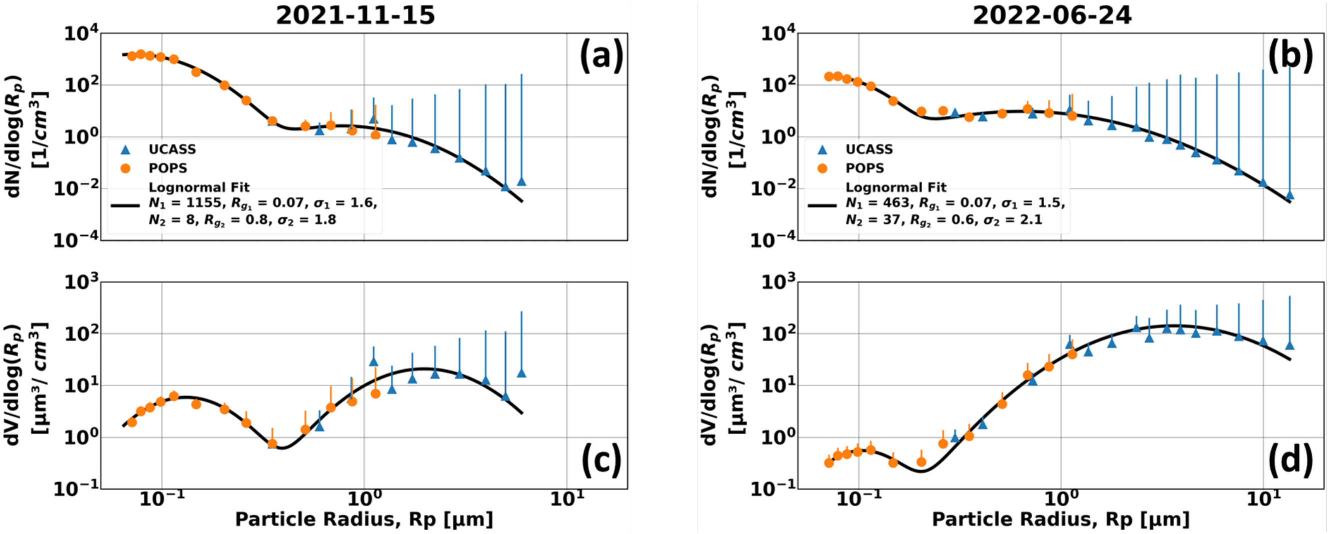

Figure 8. Number and volume size distributions for 15th November 2021 (a,c) and 24th June 2022 (b,d) at layers 1.5-2 km and 2-2.5 km a.g.l. respectively. Bi-modal log-normal fit on the data is seen with the black line. Error bars represent the standard deviation of the number size distribution in the selected altitude range. The fitting parameters for each mode of the lognormal are seen in the legend.

4.4 Comparison of PSDs

Given the differences in how the PSDs from AERONET and UAV-based measurements are expressed, it is essential to convert them to comparable units for a meaningful comparison. The AERONET PSD is column-integrated, expressed in units of $\mu\text{m}^3/\mu\text{m}^2$. In contrast, the PSDs acquired from OPCs on board UAVs are vertically resolved and expressed in units of $\mu\text{m}^3/\mu\text{m}^3$, reflecting the volume concentrations at specific altitudes.

One way to compare these different PSDs is to create column-integrated PSDs from the UAV observations. The column-integrated PSDs are calculated as:

$$\left(\frac{dV(r)}{d\log r}\right)_{col} = \int_{z_{\min}}^{z_{\max}} \frac{dV(r,z)}{d\log r}\, dz \tag{18}$$

where dz represents the height difference (10 m) between consecutive UAV-based observations.

Figure 9 compares the AERONET and column-integrated OPC PSDs. In the first case, on 15th November 2021, the observed size distributions from the UAV-based measurements closely follow the AERONET PSD between 0.2 and 2 μm, but a deviation is observed at the fine mode particles <0.2 μm where AERONET exhibits more fine particles than the UAV-based observations. In the second case, on 24th June 2022 the UAV-based PSD shows the presence of larger particles that AERONET does not

https://doi.org/10.5194/egusphere-2025-3404
Preprint. Discussion started: 29 July 2025

capture. Overall, there is a pronounced imbalance between the fine and coarse modes of the two methods. These discrepancies 445 could be attributed to the AERONET cut-off at 15 μm, which can not always be realistic for dust aerosols as seen in both demonstration cases. Furthermore, the reason for these differences may be the uncertainty in the retrieval of the volume PSD by the AERONET algorithm, and/or uncertainties associated with the OPC measurements (as discussed in Sec. 4.3.2). The impact of these differences is further investigated in the following section.

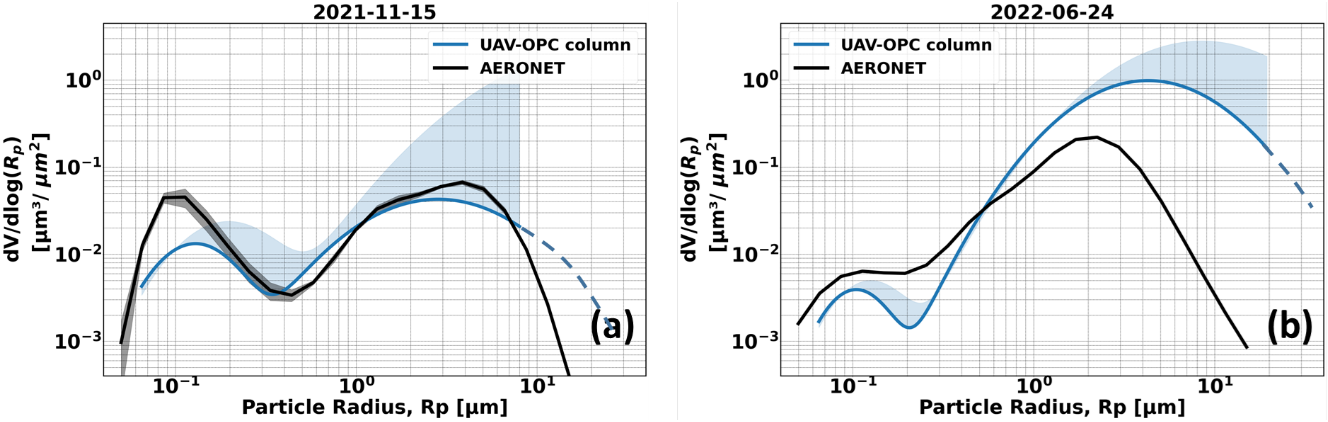

Figure 9. Column integrated volume size distributions acquired with OPCs on board UAVs, compared to AERONET for 15th November 2021 (a) and 24th June 2022 (b). The shaded area indicates the standard errors of the fitted log-normal. The dashed line corresponds to the extrapolated log-normal curve beyond the maximum observed size bin.

5 Results

450
5.1 Observed volume-to-extinction ratio

Using the formulation presented in Sect. 2, Eq. 9, the profile of the ζ parameter (volume-to-extinction ratio) is derived by combining the extinction coefficient profile acquired from the lidar measurements, with volume concentration at different heights obtained by integrating the OPC-derived PSDs. Ansmann et al. (2012) provides an overview of the volume-to-extinction conversion factor (ζ), based on observations (airborne, AERONET and lidar) (Johnson and Osborne, 2011; Osborne et al., 455 2008; Weinzierl et al., 2009; Müller et al., 2012) and models during Saharan dust events (Hess et al., 1998; Barnaba and Gobbi, 2004). In that study ζ typically ranges from 0.6 to 1.3 μm. A subsequent study by Ansmann et al. (2019b) shows ζ values based on long-term AERONET climatologies collected at desert stations around the globe. Notably, the Limassol (Cyprus) and Sal (Cabo Verde) stations reported ζ of 0.64 ± 0.08 μm and 0.64 ± 0.07 μm, respectively.

The observed ζ values for the two demonstration cases alongside the range of ζ values reported in the literature are presented 460 in Figure 10. For the 15th November 2021 case, the observed average $\zeta = 0.53 \pm 0.24$ μm (blue line) between 1.4–3.4 km a.s.l. (dust layers) is approximately $\sim 30\%$ lower than the smallest value for dust in the literature. Conversely, for the 24th June 2022 case, the observed average between 1.6–4.3 km a.s.l., and therefore considering the total dust layer depth, $\zeta = 1.14 \pm 1.01$ μm

which is similar to the values recorded before in the literature for Western Saharan cases. However, in the 1.6–3.5 km a.s.l. sublayer, where larger particles were more prevalent (see Fig. 7), the observed $\zeta = 2.02 \pm 0.80\ \mu m$ exceeds the literature maximum by approximately $\sim 21\%$.

The dash-dotted and dashed lines in Fig. 10 present the AERONET-derived ζ values for total and coarse aerosol fractions on the respective days (calculated with the method given in Ansmann et al., 2012). For 15th November 2021, the observed ζ values agree more closely with the AERONET-derived ζ for total aerosols, which is consistent with the agreement of the PSDs provided by AERONET and OPCS in Fig. 9. In contrast, for the 24 June 2022 case, both AERONET-derived ζ values underestimate the observed values by approximately $\sim 41\%$ within the 1.6–4.3 km a.s.l. range, with the discrepancy increasing to as much as $\sim 150\%$ between 1.5–3.5 km a.s.l., where larger particles were more dominant. This discrepancy aligns with the PSD comparison in Fig. 9, indicating that AERONET may underestimate coarse particles (due to the 15 μm limitation) and overestimate fine ones, which in turn affects the volume-to-extinction ratio (see Eq. 9). This highlights the potential inaccuracies of using column-averaged ζ values from AERONET without correcting for these size-dependent discrepancies. The coarse/fine mode imbalance observed on 24th June 2022, characterized by a significantly higher proportion of coarse particles, is the reason for the elevated ζ values.

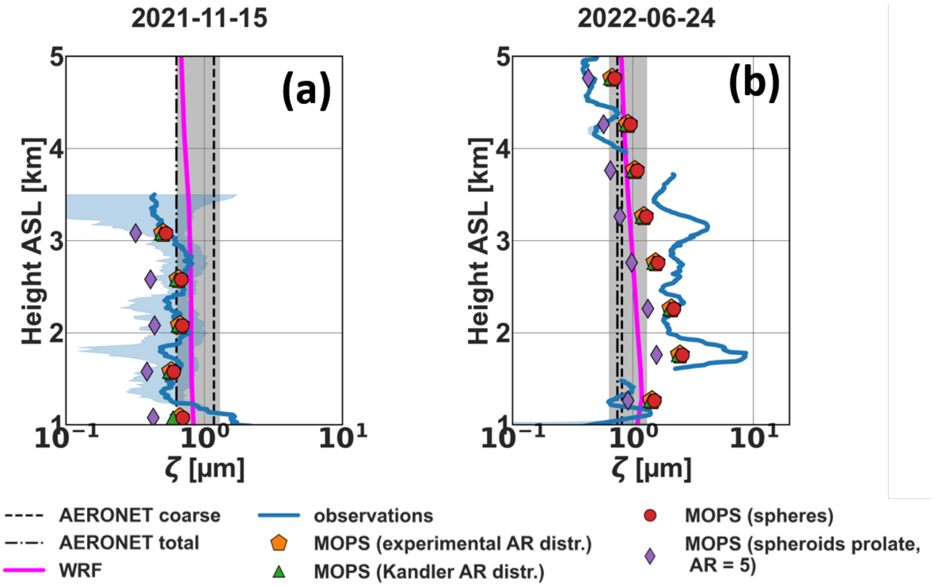

Figure 10. Observed ζ parameter (blue line) compared to MOPSMAP derived calculations for different spheroidal aspect ratios (markers) for 15th November 2021 (a) and 24th June 2022 (b). The blue shaded area corresponds to the statistical variability of ζ calculated using the lidar and UAV observations. The gray shaded area indicates the range of ζ values provided in the literature. The dashed line and dashed dotted lines denote the ζ values derived using the AERONET PSDs for total and coarse aerosols, respectively. The experimental aspect ratio distributions (lognormal) have ϵ = 1.45, σ=0.6 and ϵ = 1.44, σ=0.6 for 15th November 2021 (a) and 24th June 2022 (b) respectively. The Kanler AR distribution has ϵ = 1.45, σ=0.7

The MOPSMAP-based calculations of ζ, also shown in Fig. 10, are derived using the fitted lognormal PSDs described in Sect. 4.3.3, and refractive indices obtained from AERONET (for the real part) and SEM analysis of impactor samples collected during the flights (Kandler et al., 2009, 2018) (for the imaginary part) and a number of arbitrary values for the sphericity. The refractive indices used in the calculations were k = 1.52+0.002j and k = 1.52+0.003j for the cases 15th November 2021 and 24th June 2022, respectively (which are in both cases close to the climatological RI values for dust from Ryder et al., 2019). The MOPSMAP calculations were also performed for different RIs (real part: 1.52-1.53 and imaginary part: 0.0017-0.0056) with almost no dependency, which was expected due to the existence of coarser particles (geometric optics). Fine particles were modeled as spheres, while coarse particles were modeled as prolate spheroids with different aspect ratios: (i) aspect ratio distribution derived from the impactor samples (using SEM analysis), with ϵ and σ the center and width of the aspect ratio distribution, (ii) aspect ratio distribution from Kandler et al. (2007) ("Kandler AR distr" herein), (iii) spherical particles, and (iv) spheroids with an aspect ratio of 5. AR = 5, is an extreme value only used for comparison purposes. It must be noted that the experimental AR distributions for the two cases were very close to the distribution from Kandler et al. (2007); ϵ = 1.45,σ=0.6 and ϵ = 1.44,σ=0.6 for 15th November 2021 and 24th June 2022, and ϵ = 1.45,σ=0.7 for the Kandler distribution. At low aspect ratios the choice between oblate and prolate had negligible influence on the results.

The MOPSMAP-derived ζ values generally follow the observed profiles, though some differences remain. On November 15, 2021, using the aspect ratio distribution derived from SEM analysis of impactor samples (orange hexagons), the calculations follow well most of the observed profile, except in the 1–1.5 km a.s.l. layer, which is close to the overlap region of the lidar. The results using the Kandler AR distribution (green triangles) and spherical particles (red circles) provide similar values. For June 24, 2022, the observations up to $\sim$ 3 km, and above the marine boundary layer, align better with more spherical spheroids, even though differences are large at some altitudes e.g. $\sim$2.3 km and $\sim$3.3 km a.s.l. In the upper layers (above 3.5 km a.s.l.), spheroids with an aspect ratio of 5 show a better agreement with observations.

In Fig. 11 the observed relationship between ζ values and r_{eff} for the dates seen in Table 1 is plotted over the theoretical values (blue lines), calculated using Eq. 9, where q_{ext} is calculated using Mie theory algorithm with refractive of k = 1.52+0.003j (derived from SEM analysis of impactor samples). The theoretical lines are shown for different values of sphericity Ψ. The color of the points corresponds to the altitude of the observation, whereas observations within dust layers are marked as stars. For the Central Saharan dust case of 25th October, 2021 (Fig. 11, green box; (a)) the observations lie between the theoritical lines of sphericity with Ψ between 0.1 and 1 with some outliers with high ζ values at lower altitudes ($\leq$ 0.65 km a.s.l.). The observations at the dust layer ($\sim$1-3km) are close to the ζ values provided in the literature for dust particles, which is expected since the latter were mainly derived from Saharan dust cases. Similarly, for the second central Saharan case on the 27th October 2021 (Fig. 11, green box; (d)), the few data in the dust layer ($\sim$ 2.5km a.s.l.) are within the values provided in the literature and closer to the Ψ $\sim$0.4 sphericity line.

The observations from Middle East dust on 14th and 15th of November, 2021 (Fig. 11, black box; (b,e)), exhibit comparable characteristics and lie between the theoretical curves with sphericity between 0.1 and 0.4. The same pattern is observed for both cases with ζ and r_{eff} values decreasing for increasing altitude.

November 18, 2021 covers a wider range of r_{eff} and ζ values compared to the other cases. The measurements also span a wide range of potential sphericity, from 0.1 to 1. The color of the data points indicates that the airmasses were well mixed (vertically), as there is no clear dependence of ζ and r_{eff} with altitude. It was seen from Table 1, that the Ångström exponent presented the highest values during this day compared to the other cases, suggesting the presence of finer particles in size (something that is also confirmed by the PSDs derived from OPC measurements for this date). This is likely due to the mixing of anthropogenic pollution with dust. Bimenyimana et al. (2025) has shown that the Middle East region is the main hotspot for most PM chemical pollutants measured in Cyprus. According to HYSPLIT back-trajectory analysis for this specific case, the air masses originated from various regions in North Africa, the Middle East, and Turkey.

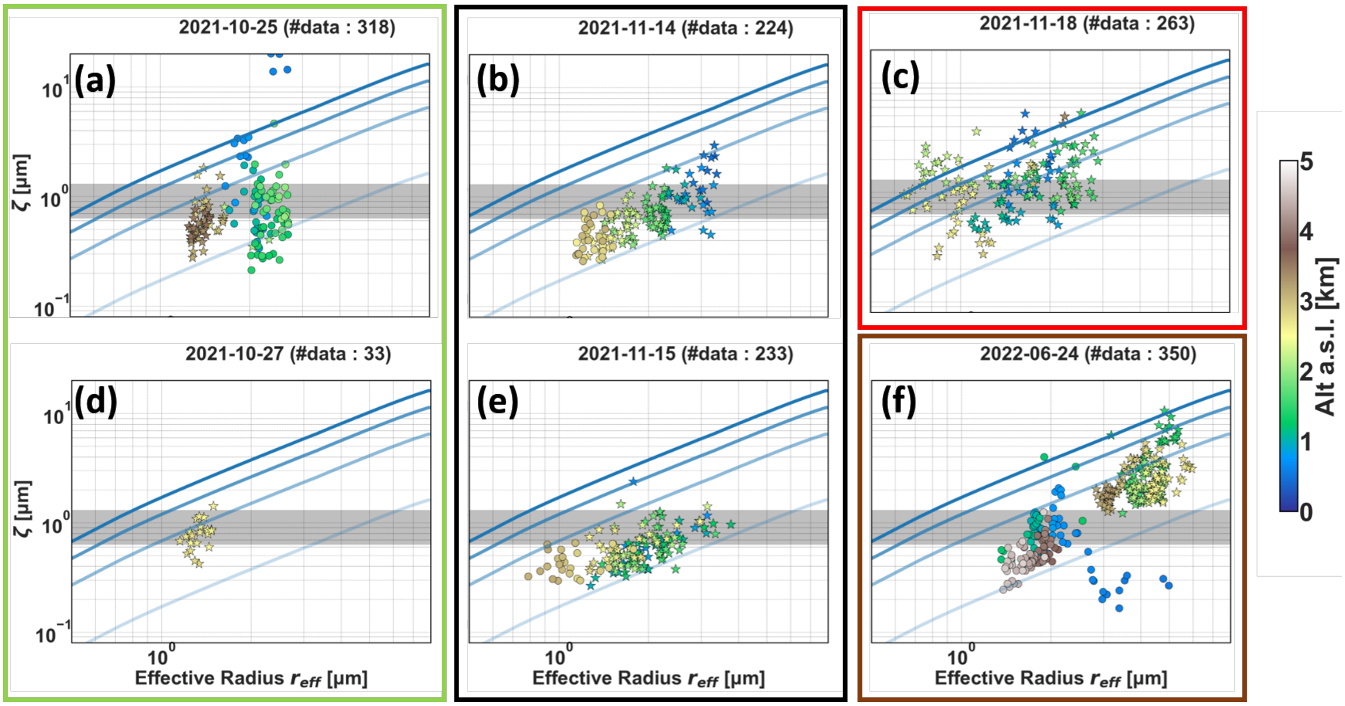

Figure 11. Scatter plots of observed ζ vs effective radius for the case studies shown in in Table 1. The theoretical blue lines (see Eq.9) have changing transparency for changing sphericity Ψ = (0.1,0.4,0.7,1) with the more intense being $\Psi = 1$. Point color indicates sampling altitude, and star-shaped markers denote observations within dust layers, as identified in Table 1. Cases are grouped by source region: green box—Central Sahara, black box—Middle East, red box—mixed origin, and brown box—Western Sahara.

On June 24, 2022, (f) the highest r_{eff} and ζ values are observed among all the days examined, due to presence of larger particles compared to other data shown here. Notably, two distinct groups of data are apparent: (1) corresponding to data inside the main dust layer ($\sim$ 1.5km-4 km a.s.l.) and (2) outside the dust layer. Some outliers in the lower part correspond to measurements inside the marine boundary layer. The observations in the dust layer mainly have a range of sphericity with $\Psi \sim$ between 0.2 and 0.7 and lie outside the range of values provided in the literature for ζ, a result that was observed in Fig. 9 as well. The observations on top and below the dust layer exhibit significantly lower r_{eff} and ζ, and are closer to the values

Table 2. Average dust ζ values for the different cases of Table 1.

Origin	Date	ζ	Average ζ
Central Sahara	2021-10-25	0.54 ± 0.29	0.63 ± 0.53
	2021-10-27	0.71 ± 0.24	
Middle East	2021-11-14	0.49 ± 0.23	0.51 ± 0.46
	2021-11-15	0.53 ± 0.24	
Mixed	2021-11-18	0.96 ± 0.79	-
West Sahara	2022-06-24	1.14± 1.01	-

provided in the literature.

It is seen from this figure that cases dominated by Middle Eastern sources (e.g., November 14 and 15, 2021) exhibit lower ζ values and a wide r_{eff} range. On the other hand Central Saharan cases have a narrower r_{eff} range. Cases from mixed origin and Western Sahara exhibit a wide range of ζ and r_{eff}. This is shown for the 18th November 2021 case, possibly due to a combination of aerosols (pollution, residual dust). For the case on 24th June 2022, the highest r_{eff} values are found, due to the presence of giant particles.

Overall, the observed values for ζ and r_{eff} for dust particles, vary significantly depending on the source regions, which can be different for the airmasses at different altitudes. In addition, a big fraction of observations at the dust layers lie outside the range of values provided for ζ in the literature, which in some cases (i.e. Cabo Verde) can be related to the limitation of AERONET and models to account for coarser and giant particles. For Middle Eastern cases, the discrepancies may also be due to the limited number of studies on dust originating from this region.

Table 2 summarizes the ζ values with their respective statistical uncertainties across the different source regions seen in Table 1. The West Saharan case exhibits the largest ζ, which is related to the higher effective radii driven by the important fraction of the coarse-mode dust. In contrast, the Middle Eastern cases show the smallest ζ values, likely due to the significant fraction of fine-mode dust.

5.2 Assessment of the WRF-Chem volume-to-extinction ratio

The WRF-Chem model set-ups described in Sect. 3.5 are used to calculate ζ for the selected cases. The modelled ζ (Eq. 19) is derived from the simulated total dust mass concentration ('TOT_DUST', $\mu g/m^3$), divided by the simulated extinction coefficients for 550 nm ('EXTCOF55', $1/km$) and the density ρ. The WRF-GOCART module models the dust PSD using five size bins, with ρ =2500 kg/m^3 for the first bin and ρ =2650 kg/m^3 for bins 2–5 (Ukhov et al., 2021).

$$\zeta_{sim} = \frac{TOT\_DUST}{EXTCOF55 \cdot \rho} \tag{19}$$

The observed and the simulated ζ are compared to the observations in Fig. 10 for the two demonstration cases on 15th November 2021, during Fall Campaign, and on 24th June 2022 during ASKOS. The WRF-Chem simulation for November 15, 2021, shows agreement within the standard deviation of the observations, with simulated ζ values being at the lower part of those reported in the literature. In contrast, for June 24, 2022, the WRF-Chem simulations align well with the ζ values reported in the literature but underestimate the observed ζ. This discrepancy is expected, as the model accounts for particles with radii up to 10 μm, whereas observations indicate the presence of particles exceeding 20 μm during this case as seen in Fig. 9 and as discussed in the previous section.

6 Conclusions

Understanding the properties of atmospheric dust and other aerosols is important for quantifying climate forcing and has broad implications across several applied domains, including air quality, human health, and solar energy production (Middleton, 2017). Atmospheric aerosol load is typically described either by mass/volume concentration or by its ability to extinguish light, depending on the observational method and application. The link between gravimetric and optical properties plays a key role in model evaluation, data assimilation, and regulatory air quality assessments. To correlate between the two expressions of the dust load, a key parameter is the volume-to-extinction ratio (another relevant parameter is the particle density, which is not examined in this study). This study demonstrates (in Eq. 9 and Fig. 11), that the volume-to-extinction ratio depends on the effective radius and shape of particles, and, for finer particles, also on the scattering efficiency, which itself is a function of geometry and refractive index.

The volume-to-extinction ratio (denoted here as ζ) is often estimated from the column-averaged particle size distribution (PSD) and aerosol optical depth derived from AERONET (Ansmann, 2011). In this way, the global coverage and consistent methodology used across the network are fully exploited. However, a known limitation of the current AERONET algorithm is that it restricts the PSD to radii below 15 μm, which can lead to underestimation of both the effective radius and ζ. In modelling studies, the ζ is instead derived from the modelled aerosol PSD. However, some models typically include aerosol particles with radii up to 10 μm, missing thus the coarse and giant mode particles which are especially relevant for mineral dust. This leads to inaccurate simulations of the dust load and its radiative effects (Adebiyi and Kok, 2020; O'Sullivan et al., 2020; Drakaki et al., 2022). Adebiyi and Kok (2020) has quantified this models' limitation, showing that it results in a significant underestimation of giant particle abundance by up to a factor of four. As a consequence of this limitation is that also in models ζ is significantly underestimated.

Recent observations from ocean-surface observations (van der Does et al., 2018) and airborne campaigns (Ryder et al., 2015, 2018) have highlighted the presence of the dust coarse and giant particles; however, these datasets remain sparse. In this study, a combined use of ground-based lidar and airborne in situ (UAV-based) observations of the PSD is presented, to derive vertically resolved values of the volume-to-extinction ratio of dust during various dust events. This research, in alignment with previous work (Estellés et al., 2018; Marenco et al., 2018; Ryder et al., 2019), confirms the observation of giant particles over the Eastern Atlantic (Cabo Verde), and this is reflected in the derived ζ.

When compared to the ζ values derived from AERONET, following the well-established method of Ansmann (2011), good agreement is found for the Middle East case, where no giant particles were observed. In contrast, significant differences, up to 150 %, are observed over the Eastern Atlantic. Similar discrepancies are evident when comparing with values reported in the literature (Ansmann et al., 2012, 2019a). Note that the findings of the present study confirm the findings by Müller et al. (2010), who reported that the effective particle radii from AERONET retrievals tend to be underestimated compared to those calculated from in-situ observations of the PSD. In contrast, the observations in Cyprus show better agreement with both AERONET-derived and literature-based values of effective radius and ζ (Figs. 10 and 11). The observed dust over Cyprus is characterised by a smaller concentration of coarse and giant particles than the dust over the Eastern Atlantic, and a larger concentration of fine particles. This suggests a more mixed aerosol type, which could be influenced by regional pollution. While Cyprus is frequently affected by Saharan dust, it is also exposed to dust outbreaks originating from the Middle East (Kezoudi 2025 et al. in preparation), which often carry not only dust, but also a significant amount of anthropogenic pollutants. Bimenyimana et al. (2025) identified the Middle East as a major source of fine particles transported to Cyprus, largely from fossil fuel combustion. Similarly, Christodoulou et al. (2023) demonstrated that emissions from this Middle East industry contribute significantly to organic aerosols and black carbon levels in Cyprus.

The evaluation of the WRF-Chem modeled ζ against observations highlighted a similar underestimation of the modeled particle size, and therefore of the ζ, for the Eastern Atlantic case. This underestimation reflects the model's limited representation of giant particles, as discussed earlier.

The influence of particle shape on the volume-to-extinction ratio has also been examined. For this, MOPSMAP optical model is used, with input of different aspect ratios and refractive indices, both derived from literature as well as by SEM analysis on the UAV-based filter samples. Near-spherical particles, with AR close to 1 (aligning well with Kandler et al., 2009), largely reproduced the observed ζ values over Cyprus. Over the Eastern Atlantic, larger discrepancies were observed. Although near-spherical shapes showed a better agreement with observations at some altitudes, simulations with higher aspect ratios provided a closer match to the observed ζ values near the top of the dust layer. These differences between events and across altitudes suggest variability in dust particle morphology, possibly due to differences in source region or ageing processes. Additionally, aerosol mixing likely plays a role in these differences; pollution over Cyprus and sea salt over Cabo Verde may both influence the optical properties, particularly those related to particle shape assumptions.

This study highlights the unique strengths of airborne measurements, notably their ability to provide in-situ insights into the dust PSDs and their variability in time and space, including coarse particles larger than $20 \mu m$, which remain underestimated by remote sensing and models. While the observations presented here are limited to a handful of vertical profiles, not general enough to establish the volume-to-extinction ratio of dust as a unique general result, they demonstrate the need to refine both observational and modelling approaches to capture the full dust size spectrum (including coarse and giant modes). As noted by Adebiyi et al. (2023), greater emphasis should be placed on synergistic airborne and ground-based measurements across a range of dust-dominated environments influenced by different source regions. The presented approach can be repeated for a number of regions near the sources (e.g. Sahara and the Middle East) and at different locations where dust is transported long-range. Ansmann et al. (2012) previously raised concerns about applying Saharan dust-derived conversion factors to other dust sources, emphasising the need for region-specific adjustments. Systematic validation and implementation of updated, regionally appropriate volume-to-extinction parameters in operational remote sensing retrievals should be aimed at. O'Sullivan et al. (2020) already discussed the need to complement the global set of observations that are currently used to constrain models (typically the AOD from AERONET and/or satellite imagers) with additional observations such as vertical distribution and PSDs. Whereas spaceborne lidar can provide information on the vertical distribution globally, PSDs require in-situ observations, e.g. from balloon-borne sensors, as also suggested in their study. The current study, based on UAV in-situ observations, represents a small but significant step in that direction.

Our study emphasises the significance of the volume-to-extinction ratio in quantifying dust using models and remote sensing and in particular when bridging between optical and gravimetric quantitative estimates. It demonstrates that the spatial and vertical variability of this parameter can lead to uncertainties when using predefined, column-averaged, or literature-based values that may not be representative of specific dust conditions.

Data availability. The data from the UAV based OPCs and lidars are available here: 10.5281/zenodo.15910856 (last access: 15th July 2025).
AERONET data are available at https://aeronet.gsfc.nasa.gov/ (last access: 15th July 2025).
The ASKOS dataset can be found here in https://evdc.esa.int/publications/askos-campaign-dataset/ (last access: 15th July 2025)

Author contributions. AP: Conceptualization, participation in field campaigns and data acquisition, data analysis and interpretation, writing–original draft; FM: Conceptualization, supervision, participation in field campaigns and data acquisition, theoretical background, placing the subject matter in the wider context; MK: UAV–OPC observations coordination, participation in field campaigns and data acquisition.; AT: Scattering calculations, critical review of scientific content; HB, AF: Lidar observations at Mindelo; KK: SEM analysis on samples; ED, EL: WRF-Chem model; All authors have contributed by writing, reviewing and editing.

Competing interests. The authors declare no conflicts of interest.

Acknowledgements. The authors acknowledge the EMME-CARE project for supporting this work under the European Union's Horizon 2020 Research and Innovation Programme (Grant Agreement No. 856612). Additionally, we acknowledge the ESA project (Contract No. 4000131861/20/NL/IA) for funding the ASKOS campaign. Part of this work was supported through a virtual mobility by the COST Action Harmonia (CA21119) supported by COST (European Cooperation in Science and Technology). We extend our gratitude to the AERONET network and to Holger Baars, Ronny Engelmannm and Philip Goloub, principal investigators of the Mindelo and Agia Marina Xyliatou stations, for maintaining the instrument operation and providing valuable data. Parts of this research has been supported by the German Federal Ministry for Economic Affairs and Energy (BMWi, grant no. 50EE1721C), the German Federal Ministry of Education and Research (BMBF) under the FONA Strategy "Research for Sustainability" (grant no. 01LK2001A), and the European Union's Horizon 2020 research and innovation program (grant nos. 739530 and 871115). Also we thank the co-authors for their contribution to this study. We sincerely thank the USRL team for their support in advancing the scientific vision through the provision and operation of their UAV fleet. In addition, we would like to thank the CAO team for ensuring the continuous operation of the remote sensing observations at Nicosia and Agia Marina

Xyliatou. Finally, many thanks are given to Cesaria Evora International Airport and the Ocean Science Centre Mindelo for their support, which has been decisive in the success of the campaign.

https://doi.org/10.5194/egusphere-2025-3404
Preprint. Discussion started: 29 July 2025

References

Adebiyi, A., Kok, J. F., Murray, B. J., Ryder, C. L., Stuut, J. B. W., Kahn, R. A., Knippertz, P., Formenti, P., Mahowald, N. M., Pérez García-Pando, C., Klose, M., Ansmann, A., Samset, B. H., Ito, A., Balkanski, Y., Di Biagio, C., Romanias, M. N., Huang, Y., and Meng, J.: A review of coarse mineral dust in the Earth system, Aeolian Research, 60, https://doi.org/10.1016/j.aeolia.2022.100849, 2023.

Adebiyi, A. A. and Kok, J. F.: Climate models miss most of the coarse dust in the atmosphere, Tech. rep., https://www.science.org, 2020.

Albrecht, B.: Aerosols, Cloud Microphysics, and Fractional Cloudiness, Science, https://doi.org/10.1126/science.245.4923.1227, 1989.

Althausen, D., Engelmann, R., Baars, H., Heese, B., Ansmann, A., Müller, D., and Komppula, M.: Portable Raman Lidar PollyXT for automated profiling of aerosol backscatter, extinction, and depolarization, J. Atmos. Ocean. Tech., 26, 2366–2378, https://doi.org/10.1175/2009JTECHA1304.1, 2009.

Ansmann, A., Seifert, P., Tesche, M., and Wandinger, U.: Profiling of fine and coarse particle mass: case studies of Saharan dust and Eyjafjallajökull/Grimsvötn volcanic plumes, Atmospheric Chemistry and Physics, 12, 9399–9415, https://doi.org/10.5194/acp-12-9399-2012, 2012.

Ansmann, A., Mamouri, R.-E., Bühl, J., Seifert, P., Engelmann, R., Hofer, J., Nisantzi, A., Atkinson, J. D., Kanji, Z. A., Sierau, B., Vrekoussis, M., and Sciare, J.: Ice-nucleating particle versus ice crystal number concentration in altocumulus and cirrus layers embedded in Saharan dust: a closure study, Atmos. Chem. Phys., 19, 15 087–15 115, https://doi.org/10.5194/acp-19-15087-2019, 2019a.

Ansmann, A., Mamouri, R.-E., Hofer, J., Baars, H., Althausen, D., and Abdullaev, S. F.: Dust mass, cloud condensation nuclei, and ice-nucleating particle profiling with polarization lidar: updated POLIPHON conversion factors from global AERONET analysis, Atmospheric Measurement Techniques, 12, 4849–4865, https://doi.org/10.5194/amt-12-4849-2019, 2019b.

Ansmann, A. e. a.: Ash and fine-mode particle mass profiles from EARLINET-AERONET observations over central Europe after the eruptions of the Eyjafjallajökull volcano in 2010, J. Geophys. Res., 116, D00U02, https://doi.org/10.1029/2010JD015567, 2011.

Antuña-Marrero, J. C., Landulfo, E., Estevan, R., Barja, B., Robock, A., Wolfram, E., Ristori, P., Clemesha, B., Zaratti, F., Forno, R., Armandillo, E., Ãlvaro E. Bastidas, Ãngel M. de Frutos Baraja, Whiteman, D. N., Quel, E., Barbosa, H. M. J., Lopes, F., Montilla-Rosero, E., and Guerrero-Rascado, J. L.: LALINET: The First Latin American-born Regional Atmospheric Observational Network, Bulletin of the American Meteorological Society, 98, 1255 – 1275, https://doi.org/10.1175/BAMS-D-15-00228.1, 2017.

Baars, H., Kanitz, T., Engelmann, R., Althausen, D., Heese, B., Komppula, M., Preißler, J., Tesche, M., Ansmann, A., and Wandinger, U. e. a.: An overview of the first decade of PollyNET: an emerging network of automated Raman-polarization lidars for continuous aerosol profiling, Atmos. Chem. Phys., 16, 5111–5137, https://doi.org/10.5194/acp-16-5111-2016, 2016.

Barnaba, F. and Gobbi, G. P.: Aerosol seasonal variability over the Mediterranean region and relative impact of maritime, continental and Saharan dust particles over the basin from MODIS data in the year 2001, Atmos. Chem. Phys., 4, 2367–2391, https://doi.org/10.5194/acp-4-2367-2004, 2004.

Barnard, J. C., Fast, J. D., Paredes-Miranda, G., Arnott, W. P., and Laskin, A.: Evaluation of the WRF-Chem "Aerosol Chemical to Aerosol Optical Properties" Module Using Data from the MILAGRO Campaign, Journal of Geophysical Research: Atmospheres, 115, D07 206, https://doi.org/10.1029/2009JD013694, 2010.

Bimenyimana, E., Sciare, J., Oikonomou, K., Iakovides, M., Pikridas, M., Vasiliadou, E., Savvides, C., and Mihalopoulos, N.: Cross-validation of methods for quantifying the contribution of local (urban) and regional sources to PM2.5 pollution: Application in the Eastern Mediterranean (Cyprus), Atmospheric Environment, 343, 120 975, https://doi.org/10.1016/j.atmosenv.2024.120975, 2025.

Bösenberg, J. and Matthias, V.: Earlinet: A European aerosol research lidar network to establish an aerosol climatology. Report. Max-Planck-Institut für Meteorologie, vol. 348, 2003.

Carslaw, K. S., Boucher, O., Spracklen, D. V., Mann, G. W., Rae, J. G. L., Woodward, S., and Kulmala, M.: A review of natural aerosol interactions and feedbacks within the Earth system, Atmospheric Chemistry and Physics, 10, 1701–1737, https://doi.org/10.5194/acp-10-1701-2010, 2010.

Chapman, E. G., Gustafson Jr., W. I., Easter, R. C., Barnard, J. C., Ghan, S. J., Pekour, M. S., and Fast, J. D.: Coupling aerosol-cloud-radiative processes in the WRF-Chem model: Investigating the radiative impact of elevated point sources, Atmospheric Chemistry and Physics, 9, 945–964, https://doi.org/10.5194/acp-9-945-2009, 2009.

Christodoulou, A., Stavroulas, I., Vrekoussis, M., Desservettaz, M., Pikridas, M., Bimenyimana, E., Kushta, J., Ivančič, M., Rigler, M., Goloub, P., Oikonomou, K., Sarda-Estève, R., Savvides, C., Afif, C., Mihalopoulos, N., Sauvage, S., and Sciare, J.: Ambient carbonaceous aerosol levels in Cyprus and the role of pollution transport from the Middle East, Atmospheric Chemistry and Physics, 23, 6431–6456, https://doi.org/10.5194/acp-23-6431-2023, 2023.

Di Biagio, C., Formenti, P., Balkanski, Y., Caponi, L., Cazaunau, M., Pangui, E., Journet, E., Nowak, S., Caquineau, S., Andreae, M. O., Kandler, K., Saeed, T., Piketh, S., Seibert, D., Williams, E., and Doussin, J.-F.: Global scale variability of the mineral dust long-wave refractive index: a new dataset of in situ measurements for climate modeling and remote sensing, Atmospheric Chemistry and Physics, 17, 1901–1929, https://doi.org/10.5194/acp-17-1901-2017, 2017.

Di Biagio, C., Formenti, P., Balkanski, Y., Caponi, L., Cazaunau, M., Pangui, E., Journet, E., Nowak, S., Andreae, M. O., Kandler, K., Saeed, T., Piketh, S., Seibert, D., Williams, E., and Doussin, J.-F.: Complex refractive indices and single-scattering albedo of global dust aerosols in the shortwave spectrum and relationship to size and iron content, Atmospheric Chemistry and Physics, 19, 15 503–15 531, https://doi.org/10.5194/acp-19-15503-2019, 2019.

Drakaki, E., Amiridis, V., Tsekeri, A., Gkikas, A., Proestakis, E., Mallios, S., Solomos, S., Spyrou, C., Marinou, E., Ryder, C. L., Bouris, D., and Katsafados, P.: Modeling coarse and giant desert dust particles, Atmospheric Chemistry and Physics, 22, 12 727–12 748, https://doi.org/10.5194/acp-22-12727-2022, 2022.

Dubovik, O. and King, M. D.: A flexible inversion algorithm for retrieval of aerosol optical properties from Sun and sky radiance measurements, Journal of Geophysical Research: Atmospheres, 105, 20 673–20 696, https://doi.org/https://doi.org/10.1029/2000JD900282, 2000.

Engelmann, R., Kanitz, T., Baars, H., Heese, B., Althausen, D., Fahrwald, A., Wandinger, U., Komppula, M., Stachlewska, I., Amiridis, V., Marinou, E., Mattis, I., Linné, H., and Ansmann, A.: The automated multiwavelength Raman polarization and water-vapor lidar PollyXT: The neXT generation, Atmos. Meas. Tech., 9, 1767–1784, https://doi.org/10.5194/amt-9-1767-2016, 2016.

Estellés, V., Marenco, F., Ryder, C., Segura, S., O'Sullivan, D., Brooke, J., Campanelli, M., Buxmann, J., and Martínez-Lozano, J. A.: Validation of AERONET and ESR/SKYNET size distributions with airborne in situ measurements in dust conditions, in: 9th International Workshop on Sand/Duststorms and Associated Dustfall, Tenerife, Spain, 22–24 May 2018, 2018.

Fast, J. D., Gustafson Jr., W. I., Easter, R. C., Zaveri, R. A., Barnard, J. C., Chapman, E. G., Grell, G. A., and Peckham, S. E.: Evolution of ozone, particulates, and aerosol direct radiative forcing in the vicinity of Houston using a fully coupled meteorology-chemistry-aerosol model, Journal of Geophysical Research: Atmospheres, 111, https://doi.org/https://doi.org/10.1029/2005JD006721, 2006.

Fehr, T., Mccarthy, W., Amiridis, V., Baars, H., von Bismarck, J., et al.: The Joint Aeolus Tropical Atlantic Campaign 2021/2022 Overview-Atmospheric Science and Satellite Validation in the Tropics, in: EGU23, the 25th EGU General Assembly, pp. EGU23–7249, Vienna and Online, Austria, https://doi.org/10.5194/egusphere-egu23-7249, insu-04472814, 2023.

Fernald, G. F.: Analysis of atmospheric lidar observations: some comments, Appl. Opt., 23, 652–653, https://doi.org/10.1364/AO.23.000652, 1984.

Fountoulakis, I., Tsekeri, A., Kazadzis, S., Amiridis, V., Nersesian, A., Tsichla, M., Proestakis, E., Gkikas, A., Papachristopoulou, K., Barlakas, V., Emde, C., and Mayer, B.: A sensitivity study on radiative effects due to the parameterization of dust optical properties in models, Atmospheric Chemistry and Physics, 24, 4915–4948, https://doi.org/10.5194/acp-24-4915-2024, 2024.

Gao, R. S., Telg, H., McLaughlin, R. J., Ciciora, S. J., Watts, L. A., Richardson, M. S., Schwarz, J. P., Perring, A. E., Thornberry, T. D., Rollins, A. W., Markovic, M. Z., Bates, T. S., Johnson, J. E., and Fahey, D. W.: A light-weight, high-sensitivity particle spectrometer for PM2.5 aerosol measurements, Aerosol Science and Technology, 50, 88–99, https://doi.org/10.1080/02786826.2015.1131809, 2016.

Gasteiger, J. and Wiegner, M.: MOPSMAP v1.0 user guide 'Modelled optical properties of ensembles of aerosol particles' https://mopsmap.net, pp. 1–20, https://doi.org/10.5281/zenodo.1284217., 2018a.

Gasteiger, J. and Wiegner, M.: MOPSMAP v1.0: A versatile tool for the modeling of aerosol optical properties, Geoscientific Model Development, 11, 2739–2762, https://doi.org/10.5194/gmd-11-2739-2018, 2018b.

Gasteiger, J., Groß, S., Freudenthaler, V., and Wiegner, M.: Volcanic ash from Iceland over Munich: mass concentration retrieved from ground-based remote sensing measurements, Atmospheric Chemistry and Physics, 11, 2209–2223, https://doi.org/10.5194/acp-11-2209-2011, 2011.

Gebauer, H., Floutsi, A. A., Haarig, M., Radenz, M., Engelmann, R., Althausen, D., Skupin, A., Ansmann, A., Zenk, C., and Baars, H.: Tropospheric sulfate from Cumbre Vieja (La Palma) observed over Cabo Verde contrasted with background conditions: a lidar case study of aerosol extinction, backscatter, depolarization and lidar ratio profiles at 355, 532 and 1064 nm, Atmospheric Chemistry and Physics, 24, 5047–5067, https://doi.org/10.5194/acp-24-5047-2024, 2024.

Ghan, S. J. and Zaveri, R. A.: Parameterization of Optical Properties for Hydrated Internally Mixed Aerosols, Journal of Geophysical Research: Atmospheres, 112, D10 201, https://doi.org/10.1029/2006JD007927, 2007.

Grell, G. A., Peckham, S. E., Schmitz, R., McKeen, S. A., Frost, G., Skamarock, W. C., and Eder, B.: Fully coupled online chemistry within the WRF model, Atmospheric Environment, 39, 6957–6975, https://doi.org/https://doi.org/10.1016/j.atmosenv.2005.04.027, 2005.

Haywood, J., Francis, P., Osborne, S., Glew, M., Loeb, N., Highwood, E., Tanré, D., Myhre, G., Formenti, P., and Hirst, E.: Radiative properties and direct radiative effect of Saharan dust measured by the C-130 aircraft during SHADE: 1. Solar spectrum, Journal of Geophysical Research: Atmospheres, 108, https://doi.org/10.1029/2002jd002687, 2003.

Hess, M., Koepke, P., and Schult, I.: Optical properties of aerosols and clouds: The software package OPAC, B. Am. Meteorol. Soc., 79, 831–844, 1998.

Hofer, J., Althausen, D., Abdullaev, S. F., Makhmudov, A. N., Nazarov, B. I., Schettler, G., Engelmann, R., Baars, H., Fomba, K. W., Müller, K., Heinold, B., Kandler, K., and Ansmann, A.: Long-term profiling of mineral dust and pollution aerosol with multiwavelength polarization Raman lidar at the Central Asian site of Dushanbe, Tajikistan: case studies, Atmos. Chem. Phys., 17, 14 559–14 577, https://doi.org/10.5194/acp-17-14559-2017, 2017.

Hofer, J., Ansmann, A., Althausen, D., Engelmann, R., Baars, H., Abdullaev, S. F., and Makhmudov, A. N.: Long-term profiling of aerosol light extinction, particle mass, cloud condensation nuclei, and ice-nucleating particle concentration over Dushanbe, Tajikistan, in Central Asia, Atmos. Chem. Phys., 20, 4695–4711, https://doi.org/10.5194/acp-20-4695-2020, 2020a.

Hofer, J., Ansmann, A., Althausen, D., Engelmann, R., Baars, H., Fomba, K. W., Wandinger, U., Abdullaev, S. F., and Makhmudov, A. N.: Optical properties of Central Asian aerosol relevant for spaceborne lidar applications and aerosol typing at 355 and 532 nm, Atmos. Chem. Phys., 20, 9265–9280, https://doi.org/10.5194/acp-20-9265-2020, 2020b.

Holben, B., Eck, T., Slutsker, I., TanrÃ©, D., Buis, J., Setzer, A., Vermote, E., Reagan, J., Kaufman, Y., Nakajima, T., Lavenu, F., Jankowiak, I., and Smirnov, A.: AERONET: A Federated Instrument Network and Data Archive for Aerosol Characterization, Remote Sensing of Environment, 66, 1–16, https://doi.org/https://doi.org/10.1016/S0034-4257(98)00031-5, 1998.

Illingworth, A. J., Barker, H. W., Beljaars, A., Ceccaldi, M., Chepfer, H., Clerbaux, N., Cole, J., DelanoÃ«, J., Domenech, C., Donovan, D. P., Fukuda, S., Hirakata, M., Hogan, R. J., Huenerbein, A., Kollias, P., Kubota, T., Nakajima, T., Nakajima, T. Y., Nishizawa, T., Ohno, Y., Okamoto, H., Oki, R., Sato, K., Satoh, M., Shephard, M. W., VelÃ¡zquez-BlÃ¡zquez, A., Wandinger, U., Wehr, T., and van Zadelhoff, G.-J.: The EarthCARE Satellite: The Next Step Forward in Global Measurements of Clouds, Aerosols, Precipitation, and Radiation, Bulletin of the American Meteorological Society, 96, 1311 – 1332, https://doi.org/10.1175/BAMS-D-12-00227.1, 2015.

IPCC: Climate Change 2021: The Physical Science Basis. Contribution of Working Group I to the Sixth Assessment Report of the Intergovernmental Panel on Climate Change, Cambridge University Press, https://doi.org/10.1017/9781009157896, 2021.

Jimenez, C., Ansmann, A., Engelmann, R., Donovan, D., Malinka, A., Schmidt, J., Seifert, P., and Wandinger, U.: The dual-field-of-view polarization lidar technique: a new concept in monitoring aerosol effects in liquid-water clouds – theoretical framework, Atmos. Chem. Phys., 20, 15 247–15 263, https://doi.org/10.5194/acp-20-15247-2020, 2020.

Johnson, B. and Osborne, S. R.: Physical and optical properties of mineral dust aerosol measured by aircraft during the GERBILS campaign, Q. J. Roy. Meteor. Soc., 137, 1117–1130, 2011.

Johnson, B., Turnbull, K., Brown, P., Burgess, R., Dorsey, J., Baran, A. J., Webster, H., Haywood, J., Cotton, R., Ulanowski, Z., Hesse, E., Woolley, A., and Rosenberg, P.: In situ observations of volcanic ash clouds from the FAAM aircraft during the eruption of EyjafjallajÃ¶kull in 2010, Journal of Geophysical Research: Atmospheres, 117, https://doi.org/https://doi.org/10.1029/2011JD016760, 2012.

Johnson, B. T., Haywood, J. M., Langridge, J. M., Darbyshire, E., Morgan, W. T., Szpek, K., Brooke, J. K., Marenco, F., Coe, H., Artaxo, P., et al.: Evaluation of biomass burning aerosols in the HadGEM3 climate model with observations from the SAMBBA field campaign, Atmospheric Chemistry and Physics, 16, 14 657–14 685, 2016.

Kandler, K., Benker, N., Bundke, U., Cuevas, E., Ebert, M., Knippertz, P., RodrÃguez, S., SchÃ¼tz, L., and Weinbruch, S.: Chemical composition and complex refractive index of Saharan Mineral Dust at Izaña, Tenerife (Spain) derived by electron microscopy, Atmospheric Environment, 41, 8058–8074, https://doi.org/https://doi.org/10.1016/j.atmosenv.2007.06.047, 2007.

Kandler, K., Schütz, L., Deutscher, C., Ebert, M., Hofmann, H., Jäckel, S., Jaenicke, R., Knippertz, P., Lieke, K., Massling, A., Petzold, A., Schladitz, A., Weinzierl, B., Wiedensohler, A., Zorn, S., and Weinbruch, S.: Size distribution, mass concentration, chemical and mineralogical composition and derived optical parameters of the boundary layer aerosol at Tinfou, Morocco, during SAMUM 2006, Tellus, Series B: Chemical and Physical Meteorology, 61, 32–50, https://doi.org/10.1111/j.1600-0889.2008.00385.x, 2009.

Kandler, K., Schneiders, K., Ebert, M., Hartmann, M., Weinbruch, S., Prass, M., and Pöhlker, C.: Composition and mixing state of atmospheric aerosols determined by electron microscopy: Method development and application to aged Saharan dust deposition in the Caribbean boundary layer, Atmospheric Chemistry and Physics, 18, 13 429–13 455, https://doi.org/10.5194/acp-18-13429-2018, 2018.

Karyampudi, V. M., Palm, S. P., Reagen, J. A., Fang, H., Grant, W. B., Hoff, R. M., Moulin, C., Pierce, H. F., Torres, O., Browell, E. V., and Melfi, S. H.: Validation of the Saharan Dust Plume Conceptual Model Using Lidar, Meteosat, and ECMWF Data, Bulletin of the American Meteorological Society, 80, 1045 – 1076, https://doi.org/10.1175/1520-0477(1999)080<1045:VOTSDP>2.0.CO;2, 1999.

Karydis, V. A., Tsimpidi, A. P., Bacer, S., Pozzer, A., Nenes, A., and Lelieveld, J.: Global impact of mineral dust on cloud droplet number concentration, Atmospheric Chemistry and Physics, 17, 5601–5621, https://doi.org/10.5194/acp-17-5601-2017, 2017.

Kezoudi, M., Keleshis, C., Antoniou, P., Biskos, G., Bronz, M., Constantinides, C., Desservettaz, M., Gao, R.-S., Girdwood, J., Harnetiaux, J., Kandler, K., Leonidou, A., Liu, Y., Lelieveld, J., Marenco, F., Mihalopoulos, N., Močnik, G., Neitola, K., Paris, J.-D., Pikridas, M., Sarda-Esteve, R., Stopford, C., Unga, F., Vrekoussis, M., and Sciare, J.: The Unmanned Systems Research Laboratory (USRL): A New Facility for UAV-Based Atmospheric Observations, Atmosphere, 12, https://doi.org/10.3390/atmos12081042, 2021a.

Kezoudi, M., Tesche, M., Smith, H., Tsekeri, A., Baars, H., Dollner, M., Estellés, V., Bühl, J., Weinzierl, B., Ulanowski, Z., Müller, D., and Amiridis, V.: Measurement report: Balloon-borne in situ profiling of Saharan dust over Cyprus with the UCASS optical particle counter, Atmospheric Chemistry and Physics, 21, 6781–6797, https://doi.org/10.5194/acp-21-6781-2021, 2021b.

Klett, J. D.: Lidar inversion with variable backscatter/extinction ratios, Appl. Opt., 24, 1638–1643, https://doi.org/10.1364/AO.25.000833, 1985.

Koch, D. and Del Genio, A. D.: Black carbon semi-direct effects on cloud cover: review and synthesis, Atmospheric Chemistry and Physics, 10, 7685–7696, https://doi.org/10.5194/acp-10-7685-2010, 2010.

Kok, J. F., Storelvmo, T., Karydis, V. A., Adebiyi, A. A., Mahowald, N. M., Evan, A. T., He, C., and Leung, D. M.: Mineral dust aerosol impacts on global climate and climate change, Nature Reviews Earth & Environment, 4, 71–86, https://doi.org/10.1038/s43017-022-00379-5, 2023.

Lieke, K., Kandler, K., Scheuvens, D., Emmel, C., Von Glahn, C., Petzold, A., Weinzierl, B., Veira, A., Ebert, M., Weinbruch, S., and SchÃ¼tz, L.: Particle chemical properties in the vertical column based on aircraft observations in the vicinity of Cape Verde Islands, Tellus B: Chemical and Physical Meteorology, https://doi.org/10.1111/j.1600-0889.2011.00553.x, 2011.

Lopatin, A., Dubovik, O., Fuertes, D., Stenchikov, G., Lapyonok, T., Veselovskii, I., Wienhold, F. G., Shevchenko, I., Hu, Q., and Parajuli, S.: Synergy processing of diverse ground-based remote sensing and in situ data using the GRASP algorithm: applications to radiometer, lidar and radiosonde observations, Atmospheric Measurement Techniques, 14, 2575–2614, https://doi.org/10.5194/amt-14-2575-2021, 2021.

Lorenz, L.: Lysbevægelsen i og uden for en af plane Lysbølger belyst Kugle, Kongelige Danske Videnskabernes Selskabs Skrifter: Naturvidenskabelig og Mathematisk Afdeling, https://books.google.com.cy/books?id=hnE7QwAACAAJ, 1890.

Mahowald, N., Albani, S., Kok, J. F., Engelstaeder, S., Scanza, R., Ward, D. S., and Flanner, M. G.: The size distribution of desert dust aerosols and its impact on the Earth system, Aeolian Research, 15, 53–71, https://doi.org/https://doi.org/10.1016/j.aeolia.2013.09.002, 2014.

Mamouri, R. E. and Ansmann, A.: Fine and coarse dust separation with polarization lidar, pp. 3717–3735, https://doi.org/10.5194/amt-7-3717-2014, 2014.

Marenco, F., Santacesaria, V., Bais, A. F., Balis, D., di Sarra, A., Papayannis, A., and Zerefos, C.: Optical properties of tropospheric aerosols determined by lidar andspectrophotometric measurements (Photochemical Activity and Solar UltravioletRadiation campaign), Appl. Opt., 36, 6875–6886, https://doi.org/10.1364/AO.36.006875, 1997.

Marenco, F., Johnson, B., Turnbull, K., Newman, S., Haywood, J., Webster, H., and Ricketts, H.: Airborne lidar observations of the 2010 EyjafjallajÃ¶kull volcanic ash plume, Journal of Geophysical Research: Atmospheres, 116, https://doi.org/https://doi.org/10.1029/2011JD016396, 2011.

Marenco, F., Ryder, C., Estellés, V., O'Sullivan, D., Brooke, J., Orgill, L., Lloyd, G., and Gallagher, M.: Unexpected vertical structure of the Saharan Air Layer and giant dust particles during AER-D, Atmospheric Chemistry and Physics, 18, 17 655–17 668, https://doi.org/10.5194/acp-18-17655-2018, 2018.

Marinou, E., Paschou, P., Tsikoudi, I., Tsekeri, A., Daskalopoulou, V., Kouklaki, D., Siomos, N., Spanakis-Misirlis, V., Voudouri, K. A., Georgiou, T., Drakaki, E., Kampouri, A., Papachristopoulou, K., Mavropoulou, I., Mallios, S., Proestakis, E., Gkikas, A., Koutsoupi, I., Raptis, I. P., Kazadzis, S., Baars, H., Floutsi, A., Pirloaga, R., Nemuc, A., Marenco, F., Kezoudi, M., Papetta, A., Močnik, G., Díez, J. Y., Ryder, C. L., Ratcliffe, N., Kandler, K., Sudharaj, A., and Amiridis, V.: An Overview of the ASKOS Campaign in Cabo Verde, p. 200, https://doi.org/10.3390/environsciproc2023026200, 2023.

Mei, F., McMeeking, G., Pekour, M., Gao, R.-S., Kulkarni, G., China, S., Telg, H., Dexheimer, D., Tomlinson, J., and Schmid, B.: Performance Assessment of Portable Optical Particle Spectrometer (POPS), Sensors, 20, https://doi.org/10.3390/s20216294, 2020.

Middleton, N.: Desert dust hazards: A global review, Aeolian Research, 24, 53–63, https://doi.org/https://doi.org/10.1016/j.aeolia.2016.12.001, 2017.

Mie, G.: BeitrÃ¤ge zur Optik trÃ¼ber Medien, speziell kolloidaler MetallÃ¶sungen, Annalen der Physik, 330, 377–445, https://doi.org/https://doi.org/10.1002/andp.19083300302, 1908.

Moteki, N.: Climate-relevant properties of black carbon aerosols revealed by in situ measurements: a review, Progress in Earth and Planetary Science, https://doi.org/10.1186/s40645-023-00544-4, 2023.

Müller, T., Weinzierl, B., Petzold, A., Kandler, K., Ansmann, A., Mller, D., Tesche, M., Freudenthaler, V., Esselborn, M., Heese, B., Althausen, D., Schladitz, A., Otto, S., and Knippertz, P.: Mineral dust observed with AERONET Sun photometer, Raman lidar, and in situ instruments during SAMUM 2006: Shape-independent particle properties, Journal of Geophysical Research Atmospheres, 115, 1–18, https://doi.org/10.1029/2009JD012520, 2010.

Müller, D., Veselovskii, I., Kolgotin, A., Tesche, M., Ansmann, A., and Dubovik, O.: Vertical profiles of pure dust (SAMUM-1) and mixed-smoke-dust plumes (SAMUM 2008) inferred from inversion of multiwavelength Raman/polarization lidar data and comparison to AERONET retrievals, Appl. Opt., submitted, 2012.

Nakajima, T., Yoon, S.-C., Ramanathan, V., Shi, G.-Y., Takemura, T., Higurashi, A., Takamura, T., Aoki, K., Sohn, B.-J., Kim, S.-W., Tsuruta, H., Sugimoto, N., Shimizu, A., Tanimoto, H., Sawa, Y., Lin, N.-H., Lee, C.-T., Goto, D., and Schutgens, N.: Overview of the Atmospheric Brown Cloud East Asian Regional Experiment 2005 and a study of the aerosol direct radiative forcing in east Asia, Journal of Geophysical Research: Atmospheres, 112, https://doi.org/https://doi.org/10.1029/2007JD009009, 2007.

Osborne, S. R., Johnson, B. T., Haywood, J. M., Baran, A. J., Harrison, M. A. J., and McConnell, C. L.: Physical and optical properties of mineral dust aerosol during the Dust and Biomass-burning Experiment, J. Geophys. Res., 113, D00C03, https://doi.org/10.1029/2007JD009551, 2008.

O'Sullivan, D., Marenco, F., Ryder, C. L., Pradhan, Y., Kipling, Z., Johnson, B., Benedetti, A., Brooks, M., McGill, M., Yorks, J., and Selmer, P.: Models transport Saharan dust too low in the atmosphere: A comparison of the MetUM and CAMS forecasts with observations, Atmospheric Chemistry and Physics, 20, 12 955–12 982, https://doi.org/10.5194/acp-20-12955-2020, 2020.

Papetta, A., Marenco, F., Kezoudi, M., Mamouri, R.-E., Nisantzi, A., Baars, H., Popovici, I. E., Goloub, P., Victori, S., and Sciare, J.: Lidar depolarization characterization using a reference system, Atmos. Meas. Tech., 17, 1721–1738, https://doi.org/10.5194/amt-17-1721-2024, 2024.

Paschou, P., Siomos, N., Tsekeri, A., Louridas, A., Georgoussis, G., Freudenthaler, V., Binietoglou, I., Tsaknakis, G., Tavernarakis, A., Evangelatos, C., von Bismarck, J., Kanitz, T., Meleti, C., Marinou, E., and Amiridis, V.: The eVe reference polarisation lidar system for Cal/Val of Aeolus L2A product, Atmos. Meas. Tech. Discuss., 2021, 1–37, https://amt.copernicus.org/preprints/amt-2021-268/%0Ahttps://amt.copernicus.org/preprints/amt-2021-268/amt-2021-268.pdf, 2021.

Prospero, J. M., Collard, F.-X., MoliniÃ©, J., and Jeannot, A.: Characterizing the annual cycle of African dust transport to the Caribbean Basin and South America and its impact on the environment and air quality, Global Biogeochemical Cycles, 28, 757–773, https://doi.org/https://doi.org/10.1002/2013GB004802, 2014.

Robock, A.: Volcanic eruptions and climate, https://doi.org/10.1029/1998rg000054, 2000.

Ryder, C., Rosenberg, P., Brindley, H., Highwood, E., Marsham, J., Parker, D., Todd, M., et al.: Advances in understanding mineral dust and boundary layer processes over the Sahara from Fennec aircraft observations, Atmospheric Chemistry and Physics, 15, 8479–8520, 2015.

Ryder, C. L., Marenco, F., Brooke, J. K., Estelles, V., Cotton, R., Formenti, P., McQuaid, J. B., Price, H. C., Liu, D., Ausset, P., Rosenberg, P. D., Taylor, J. W., Choularton, T., Bower, K., Coe, H., Gallagher, M., Crosier, J., Lloyd, G., Highwood, E. J., and Murray, B. J.: Coarse-mode mineral dust size distributions, composition and optical properties from AER-D aircraft measurements over the tropical eastern Atlantic, Atmospheric Chemistry and Physics, 18, 17 225–17 257, https://doi.org/10.5194/acp-18-17225-2018, 2018.

Ryder, C. L., Highwood, E. J., Walser, A., Seibert, P., Philipp, A., and Weinzierl, B.: Coarse and giant particles are ubiquitous in Saharan dust export regions and are radiatively significant over the Sahara, Atmos. Chem. Phys., 19, 15 353–15 376, https://doi.org/10.5194/acp-19-15353-2019, 2019.

Schumann, U., Mayer, B., Gierens, K., Unterstrasser, S., Jessberger, P., Petzold, A., Voigt, C., and Gayet, J. F.: Effective radius of ice particles in cirrus and contrails, Journal of the Atmospheric Sciences, 68, 300–321, https://doi.org/10.1175/2010JAS3562.1, 2011.

Seinfeld, J. H., Pandis, and N., S.: Atmospheric chemistry and physics : from air pollution to climate change, J. Wiley, ISBN 0471720178, 2006.

Smith, H. R., Ulanowski, Z., Kaye, P. H., Hirst, E., Stanley, W., Kaye, R., Wieser, A., Stopford, C., Kezoudi, M., Girdwood, J., Greenaway, R., and Mackenzie, R.: The Universal Cloud and Aerosol Sounding System (UCASS): a low-cost miniature optical particle counter for use in dropsonde or balloon-borne sounding systems, Atmospheric Measurement Techniques, 12, 6579–6599, https://doi.org/10.5194/amt-12-6579-2019, 2019.

Stein, A. F., Draxler, R. R., Rolph, G. D., Stunder, B. J. B., Cohen, M. D., and Ngan, F.: NOAA's HYSPLIT Atmospheric Transport and Dispersion Modeling System, Bulletin of the American Meteorological Society, 96, 2059–2077, https://doi.org/10.1175/BAMS-D-14-00110.1, 2015.

Tsamalis, C., Chédin, A., Pelon, J., and Capelle, V.: The seasonal vertical distribution of the saharan air layer and its modulation by the wind, Atmospheric Chemistry and Physics, 13, 11 235–11 257, https://doi.org/10.5194/acp-13-11235-2013, 2013.

Tsekeri, A., Gialitaki, A., Di Paolantonio, M., Dionisi, D., Liberti, G. L., Fernandes, A., Szkop, A., Pietruczuk, A., Pérez-Ramírez, D., Granados Muñoz, M. J., Guerrero-Rascado, J. L., Alados-Arboledas, L., Bermejo Pantaleón, D., Bravo-Aranda, J. A., Kampouri, A., Marinou, E., Amiridis, V., Sicard, M., Comerón, A., Muñoz Porcar, C., Rodríguez-Gómez, A., Romano, S., Perrone, M. R., Shang, X., Komppula, M., Mamouri, R.-E., Nisantzi, A., Hadjimitsis, D., Navas-Guzmán, F., Haefele, A., Szczepanik, D., Tomczak, A., Stachlewska, I. S., Belegante, L., Nicolae, D., Voudouri, K. A., Balis, D., Floutsi, A. A., Baars, H., Miladi, L., Pascal, N., Dubovik, O., and Lopatin, A.: Combined sun-photometer–lidar inversion: lessons learned during the EARLINET/ACTRIS COVID-19 campaign, Atmospheric Measurement Techniques, 16, 6025–6050, https://doi.org/10.5194/amt-16-6025-2023, 2023.

Turnbull, K., Johnson, B., Marenco, F., Haywood, J., Minikin, A., Weinzierl, B., Schlager, H., Schumann, U., Leadbetter, S., and Woolley, A.: A case study of observations of volcanic ash from the Eyjafjallajökull eruption: 1. In situ airborne observations, Journal of Geophysical Research: Atmospheres, 117, 2012.

Ukhov, A., Ahmadov, R., Grell, G., and Stenchikov, G.: Improving dust simulations in WRF-Chem v4.1.3 coupled with the GOCART aerosol module, Geoscientific Model Development, 14, 473–493, https://doi.org/10.5194/gmd-14-473-2021, 2021.

Van de Hulst, H. C.: Light Scattering by Small Particles, John Wiley and Sons, https://doi.org/10.1063/1.3060205, 1957.

van der Does, M., Knippertz, P., Zschenderlein, P., Harrison, R. G., and Stuut, J.-B. W.: The mysterious long-range transport of giant mineral dust particles, Science Advances, 4, eaau2768, https://doi.org/10.1126/sciadv.aau2768, 2018.

Wadell, H.: Volume, Shape, and Roundness of Quartz Particles, The Journal of Geology, https://doi.org/10.1086/624298, 1935.

Weinzierl, B., Petzold, A., Esselborn, M., Wirth, M., Rasp, K., Kandler, K., Schütz, L., Koepke, P., and Fiebig, M.: Airborne measurements of dust layer properties, particle size distribution and mixing state of Saharan dust during SAMUM 2006, Tellus B, 61, 96–117, https://doi.org/10.1111/j.1600-0889.2008.00392.x, 2009.

Welton, E. J., Campbell, J. R., Spinhirne, J. D., and III, V. S. S.: Global monitoring of clouds and aerosols using a network of micropulse lidar systems, in: Lidar Remote Sensing for Industry and Environment Monitoring, edited by Singh, U. N., Asai, K., Ogawa, T., Singh, U. N., Itabe, T., and Sugimoto, N., vol. 4153, pp. 151 – 158, International Society for Optics and Photonics, SPIE, https://doi.org/10.1117/12.417040, 2001.

Winker, D. M., Vaughan, M. A., Omar, A., Hu, Y., Powell, K. A., Liu, Z., Hunt, W. H., and Young, S. A.: Overview of the CALIPSO Mission and CALIOP Data Processing Algorithms, Journal of Atmospheric and Oceanic Technology, 26, 2310 – 2323, https://doi.org/10.1175/2009JTECHA1281.1, 2009.

Zaehle, S., Ciais, P., Friend, A. D., and Prieur, V.: Carbon benefits of anthropogenic reactive nitrogen offset by nitrous oxide emissions, Nature Geoscience, https://doi.org/10.1038/ngeo1207, 2011.

Zhao, G., Li, F., and Zhao, C.: Determination of the refractive index of ambient aerosols, Atmospheric Environment, 240, 117 800, https://doi.org/https://doi.org/10.1016/j.atmosenv.2020.117800, 2020.